Acoustic imaging of large structures at low frequencies

Department of Electronic Systems
Acoustics Specialisation
4th semester
Aalborg University 2009
Group 09gr1060

AALBORG UNIVERSITY

Department of Electronic Systems
Section of Acoustics
Fredriks Bajers Vej 7
http://es.aau.dk/sections/acoustics/

Title:

Acoustic imaging of large structures at low frequencies

Theme:

Noise source identification

Project period:

E10, spring semester 2009

Project group:

09gr1060

Participants:

Estrella Merino Siles
Ignacio Pérez Pablos

Supervisor:

Christian Sejer Pedersen

Copies: 5

Enclosures: CD

Date of completion: June 3^{th}, 2009

Abstract:

This thesis concerns the investigation of the optimal solution to perform acoustic imaging of large structures at low frequencies, within the framework of wind turbines.
Beamforming is found to be a suitable method to perform acoustic imaging of wind turbines. The relevance of the measurement distance and size of the wind turbine, as well as the geometrical disposition of the microphones within the array are analysed.
An ideal virtual scenario is generated based on some assumptions. It is used to simulate a beamformer, create acoustic images and evaluate the results.
Four different array geometries, namely grid, X-cross, radial and spiral array are analysed and simulated. Their optimum parameters, i.e. number of microphones and array size, are determined in order to fulfil certain frequency range, resolution and dynamic range requirements.
An optimized radial array arises as a good compromise between acoustic image quality and practical implementation. However, the array sizes to perform the acoustic imaging of large structures at low frequencies are rather large, and would present several limitations in a practical application.

Estrella Merino Siles
<emsiles@es.aau.dk>

Ignacio Pérez Pablos
<nachete@es.aau.dk>

Preface

This master thesis is written by project group 09gr1060 at the Section of Acoustics, Department of Electronic Systems at Aalborg University during the 4rd semester of the master programme in the period spanning from February 1st, 2009 to June 3rd, 2009. The thesis concerns the investigation of the optimal method to perform acoustic imaging of large structures at low frequencies, within the framework of wind turbines.
The report is aimed at people with knowledge equivalent to the teaching on the 4th semester master programme in acoustics. The project "Acoustic imaging of large structures at low frequencies" has been proposed by Christian Sejer Pedersen.

The reader should pay attention to the following on perusal of this report:

- The report is divided into two major parts:
  - The main report which is divided into numbered chapters.
  - The appendices which are arranged alphabetically.
- Figures, tables and equations are enumerated consecutively according to the chapter number. Hence, the first figure in chapter one is named figure 1.1, the second figure figure 1.2 and so on.
- The Harvard method is used for citation. The bibliography can be found after the main report.
- The CD contains data sheets, test signals, internet sources and MatLab scripts used in this project.

Aalborg University, June 3rd 2009.

Table of Contents

List of Abbreviations

FWHM	Full-Width Half-Maximum
HIE	Hemholtz Integral Equation
NAH	Near-field Acoustic Holography
NS-STSF	Non-stationary Spatial Transformations of Sound Fields
NSI	Noise Source Identification
STSF	Spatial Transformations of Sound Fields
TDH	Time Domain Holography
VAD	Vibroacoustic Disease
WTS	Wind Turbine Syndrome

Chapter 1

Introduction

Wind power is the fastest growing energy source nowadays [Wind Power Database, 2009]. The upcoming absence of natural resources is now a matter of concern while nuclear energy is being rejected by politicians and public opinion in many countries. These facts are motivating the great growth of this clean, renewable and effective energy source.

The advantages of wind energy and their cost-effectiveness are well confirmed today, and many countries expect to increase substantially their wind power production in the following years. In fact, according to the forecast, the world wind power production might be doubled in four years [Wind Power Database, 2009]. This causes a growing concern in the environmental impact of wind turbine installations as more and more wind farms are being placed close to populated areas. Even thought they are becoming quieter with the advance of technology, their noise is still of concern for both industry and neighbours.

Problems associated with wind turbine noise and the subsequent necessity to fulfil the local noise legislation can slow down the progression of wind energy. Firstly, limiting the geographical expansion of the farms; secondly, forcing the energy companies to decrease the output power capacity of the farms, causing an impact in their economical efficiency. Besides, there is an increasing concern about their low frequency radiation and its impact on human health, some studies report problems as the so-called vibroacoustic disease (VAD) and the wind turbine syndrome (WTS). Despite they have not been totally accepted by the scientific community, they still create controversy.

Hence, it is important to comprehend the acoustic behaviour of wind turbines to minimize the aforementioned problems. Their main noise mechanisms are described in literature [Wagner et al., 1996] and measurements have been done to obtain more knowledge about their radiation levels, frequency characteristics and directivity. More recently, acoustic imaging techniques have been used to localize the actual noise sources of large wind turbines.

Such acoustic images, based on microphone array measurements, provide a better understanding of the noise radiation of the different parts of a wind turbine: tower, nacelle and blades.

K. Haddad and V. Benoit introduced a measurement technique based on acoustic imaging in the field of wind turbine noise [Haddad and Benoit, 2005]. They used a measurement system based on a method called beamforming. It allowed localizing spatially, both in time and frequency, which parts of the wind turbine contribute to the overall noise radiation.

S. Oerlemans and B. Méndez López performed array measurements in a medium-large wind turbine . They obtained acoustic images of the entire wind turbine from 500 Hz up to 2000 Hz by means of beamforming technique and drew conclusions regarding the predominant noise sources.

However, the previous studies have not considered acoustic imaging in the low frequency range, i.e. below 200 Hz. Effects occurring below the mentioned frequency have not been widely documented, and their understanding becomes highly valuable for further investigation. For instance, it might help to better accept or reject the low frequency health problems ascribed to large wind turbines or to define their vertical directivity more accurately.

The objective of this study is to investigate the optimal solution to perform acoustic imaging of large structures in low frequencies, within the framework of wind turbines. Conclusions will be drawn regarding the effectiveness and limitations of such measurement method.

Chapter 2

Problem Description

This chapter contains a brief description of a wind turbine and its main noise mechanisms. Besides, the scope of the project is defined.

2.1 Project Scope

This master thesis concerns the investigation of the optimal method to perform the identification of noise sources in large structures at low frequencies, within the framework of wind turbines.

The selection of the most suitable method and its design, together with the understanding and argumentation of its limitations, constitute the core of this thesis. Therefore, it is not objective of this study to present an analysis and draw conclusions of wind turbine noise.

2.2 Scenario: The Wind Turbine

A simple model of a wind turbine consist of a tower, a nacelle and three blades that rotate around a hub standing out the nacelle. The nacelle contains the gearbox and the generator. A basic wind turbine model can be seen in figure 2.1. The area of the circle described by the rotor determines the energy provided by the wind turbine [Danish Wind Industry Association, 2009]. Figure 2.2 shows the relationship between rotor diameter and power. The hub height can typically range from 40 to 160 m, whereas the rotor diameters ranges from 50 to 130 m.

Two main noise sources can be identified in a wind turbine: the blades passing through the air, and the nacelle, comprising the gearbox and the generator. Noise from the blades

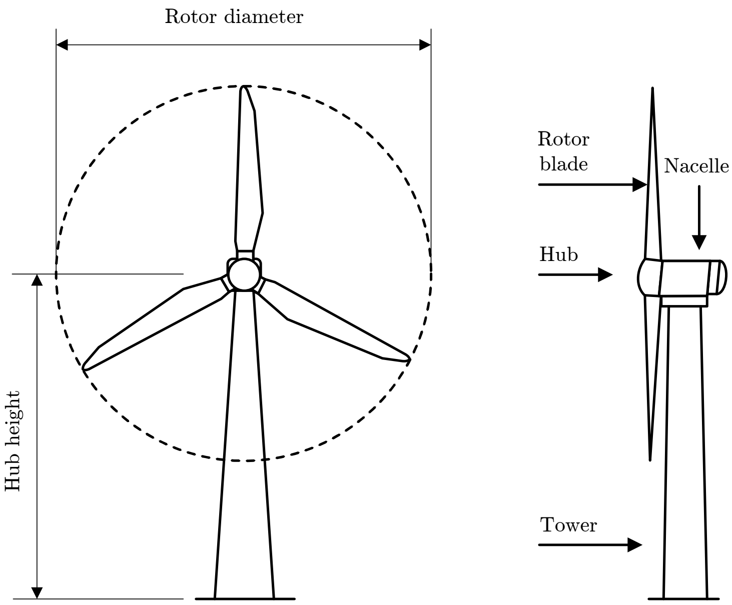

Figure 2.1: Wind turbine main parts, front and size view.

can be minimised in the design stage, whereas noise from the gearbox and generator can be minimised by isolating the nacelle [British Wind Energy Association, 2000].

The noise mechanisms of an operating wind turbine can be divided into mechanical and aerodynamic.

Mechanical noise It is originated from the motion of mechanical components, such as the gearbox, generator or cooling fans. The tower, hub and rotor transmit and radiate the noise, both in the air and the structure. Since it is associated with the rotation of the parts, it has a tonal tendency albeit it can have a broadband component [Wagner et al., 1996].

Aerodynamic noise It is caused by the air flow around the blades. It typically increases with the rotor speed (blade passing frequency). It is the largest noise source of a wind turbine, and it normally has broadband characteristics. The interaction between the tower and the passing blades causes air flow changes, which generates low frequency noise.

This low frequency noise is more prominent when the blades are located *downwind*† of the tower, since a strong pulse when the blade passes behind the tower is generated. Mostly to solve this problem, modern wind turbines have their blades *upwind* of the tower and a

†In this case, the wind strikes the the rotor from the back, i.e. it passes by the tower first. This turbines were commonly used in the USA in the 1980s.

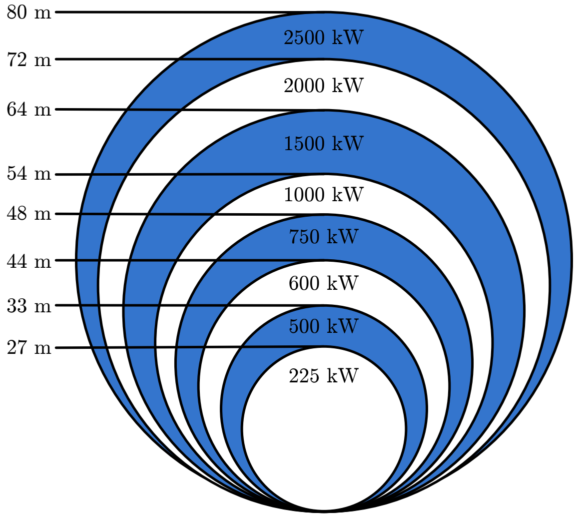

Figure 2.2: Relationship between rotor diameter and power provided by a wind turbine. Based on [Danish Wind Industry Association, 2009].

larger distance blade-tower, so as to minimize their interaction effect and the subsequent generation of high pressure levels at low frequencies. [British Wind Energy Association, 2005]

Nevertheless, according to [Rogers and Manwell, 2004], mechanical broadband and tonal noise has been reduced considerably in the design of large wind turbines recently. Hence, noise of modern wind turbines is mostly dominated by broadband aerodynamic noise.

Further analysis of the noise mechanisms of wind turbines are out of the scope of this thesis. Should the reader need a more thorough explanation about this topic, it can be found in [Wagner et al., 1996].

2.3 Problem Formulation

For the investigation of the optimal method to evaluate low-frequency noise radiation of large structures, such as wind turbines, the following questions should be solved:

- Which methods exists for such purpose?
- Which one is the most suitable for this practical application?
- Which benefits and limitations has this method for this case?
- How the different parameters affect the final results?

Chapter 3

Noise Source Identification Techniques

Noise source identification (NSI) comprises a group of different methods typically used to identify the precedence of the noise from industrial products. Identification of noise sources and characterization of their acoustic emissions (in level, frequency components and directivity) is highly valuable for the industrial sector to acoustically improve processes and products.

The output given by these techniques often consists of a representation of the object under study and a superimposed mapping with the magnitude of a certain acoustic parameter. This is called an *acoustic image*. Figure 3.1 shows an example of an acoustic image

Figure 3.1: Acoustic image generated by means of beamforming technique. Acoustic analysis software Type 7768 from Brüel & Kjær [Brüel&Kjær, 2004].

Each method presents its own operation and technical aspects with limitations in object size, measurement distance, frequency range and resolution; along with other practical issues. Therefore, it is important to carry out a comparison to select the most appropriate for the current purpose.

There exists a wide variety of techniques and implementations despite only some of them are considered for the purpose of this project, only two dimensional array based holography methods to be precise. Their descriptions are based on reviews given in [Ginn et al., 2003], [Brüel&Kjær, 1989], [Brüel&Kjær, 2000] and [Brüel&Kjær, 2004].

3.1 STSF - Spatial Transformation of Sound Fields

This technique is based on measurements taken with a two dimensional microphone array where the data acquired can be transformed to any parallel plane at any distance to the source.

Acoustic pressure is acquired by the microphone array in a measurement plane at a certain distance. This data is subsequently convolved with a two dimensional propagation matrix in order to obtain a pressure map in a desired calculation plane. This parallel plane can be calculated either closer of further to the source.

Stationary Source When measuring stationary noise, *cross-spectral holography* is used. It allows a scanning measurement technique with a scan array of smaller dimensions and using some reference microphones. It provides a complete mathematical model of the sound field from the source surface to infinite distance by using both *Near-field acoustic holography* (NAH) and *Hemholtz' integral equation* (HIE). Pressure, particle velocity and intensity can be mapped in near-field by means of NAH; whilst directivity and pressure level along a line can be calculated for far-field by means of HIE. Figure 3.2 depicts the STSF principle of operation, it shows calculation planes for both near and far field together with their corresponding calculation technique, NAH or HIE.

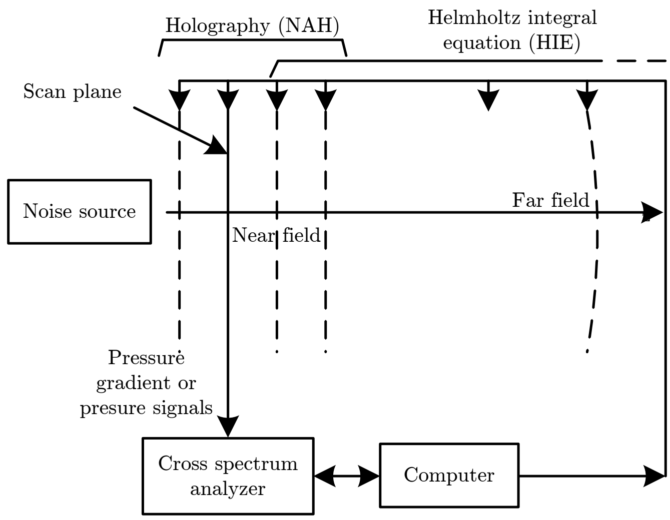

Figure 3.2: Principle of the STSF. Based on [Brüel&Kjær, 1989].

Non-stationary Source In case of a non-stationary noise source, *time domain holography* (TDH) is used instead. The non-stationary STSF (NS-STSF) technique requires a full scale measurement array covering the whole source. It provides with a sequence of pressure maps over time and shows both when and where the noise is radiated, as depicted in figure 3.3.

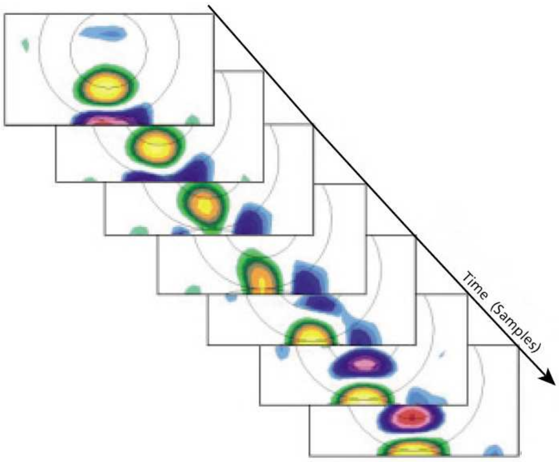

Figure 3.3: Combined space and time acoustic imaging [Brüel&Kjær, 2000].

3.1.1 Requirements

- Two dimensional spatial Fourier transform is used in order to make convolution faster by multiplication in frequency. As a consequence, the measurement points must form a rectangular grid.
- In case of non-stationary noise, the measurement area must cover the entire sound source, plus a certain solid angle away from the source.
- The spatial sampling interval, i.e. the distance between microphones, should be less than half a wavelength of the maximum frequency of interest.
- The resolution is half a wavelength for high frequencies and the measurement distance for low frequencies.

3.1.2 Advantages

- Easy of use, fast and reliable.
- Excellent spatial and temporal (NS-STSF) resolution.
- Provides a complete 3D calibrated description of the sound field both in near and far field: pressure, velocity, intensity, etc.

3.1.3 Disadvantages

- Limited frequency range, depending on the distance between microphones. Typically valid up to 6.4 kHz.
- Scanning array technique is only valid for non-stationary sources, otherwise a large amount of microphones and array dimensions might be needed.
- Measurement array must be placed near the source, therefore the noise source must be totally accessible.

Due to these facts, this technique is mostly suited for mid-low frequencies (6 kHz maximum) and its operation is limited to near-field measurements.

3.2 Beamforming

Beamforming entails the use of a two dimensional microphone array working as a *camera* or *antenna*, in the sense that it is tuned to focus on different points of the measured object. It can provide acoustic images of large structures at relatively large distances, with a useful opening angle of 60°.

This technique uses the principle of delay-and-sum[†]. A two dimensional array of microphones is used for the acquisition, and signals are subsequently processed to determine which directions of propagation are contributing to the recorded level, i.e. where the sound is actually coming from. By optimally setting the microphone delays, directivity is changed and a narrow main lobe can be steered to point a certain direction. A sound pressure level map can be obtained with information of the relative radiation levels in space and time.

The resolution of the beamformer is proportional to the array diameter and inversely proportional to the wavelength and measurement distance. It degrades substantially when the off-axis angle excess 30°. The design procedure of a beamformer starts by defining the frequency range of interest and the resolution needed, this determines the number of microphones, size of the array and measurement distance. It is important to reduce the side lobes of the directivity pattern as much as possible, thereby avoiding the presence of *ghost images* as a product of them. For this purpose, different designs exist with circular, rectangular or random arrangements among others. The study of such geometries and their performance in suppressing aliasing is a part of the design.

[†]This concept will be cover in detailed in chapter 4.

3.2.1 Requirements

- Resolution is function of wavelength, measurement distance and array size. Then to obtain sufficient resolution at low frequencies, a large array might be needed and placed sufficiently close to the source.
- All microphones must record simultaneously, therefore a full scale array and a multichannel data acquisition system are required.

3.2.2 Advantages

- Fast technique where all channels are recorded simultaneously.
- Possibility of measuring large structures, with a 60° opening angle.
- Large frequency range up to high frequencies (20 kHz).
- Good resolution in middle and high frequencies.
- Measurements can be performed in far-field. That allows measuring large structures at a certain distance.

3.2.3 Disadvantages

- Sound pressure maps are not calibrated, providing only relative levels at the array position.
- Resolution degrades with the steering angle, the maximum opening angle is 60°, therefore minimum distance source-array is limited.

Due to these characteristics, this technique is mostly used for high frequencies, where the best resolution is obtained, and for far-field applications where the source surface is not accessible.

3.3 Discussion

It has been seen that each technique has its own peculiarities, hence they has to be selected depending on the application. STST performs better in low frequencies, as it presents better resolution, although it requires a large array and a huge amount of microphones in order to cover the whole structure. In the case of a large wind turbine, where the sound is periodic, but not stationary, scanning measurements cannot be used. Therefore this technique is obviously discarded as it would require the use of, at least, 100 m array with hundreds of microphones. Besides it would have to be placed very close to the source which is not often accessible.

Beamforming, however, presents some conditions that facilitate the measurements. Firstly, it does not require to cover the whole structure with microphones, hence, less amount of them would be needed and the array surface could have a reasonable size. Secondly, it is designed to measure at a distance from the structure, then accessibility problems can be solved.

Those practical facts force the selection of beamforming as the suitable technique for measuring structures with the characteristics of large wind turbines, that are not accessible for near-field measurements and present non-stationary noise radiation. Nevertheless, resolution in low frequencies is severely decreased. Then, a solution to achieve enough spatial resolution for the assessment of wind turbines noise radiation must be found.

Chapter 4

Beamforming

Once the benefits and limitations of beamforming have been discussed in chapter 3, its operation is explained in this chapter. Before starting with beamforming concept and main theory, a brief review of *apertures* and sensor arrays is given. This review is an introduction for the beamforming delay-and-sum theory described next. The different peculiarities of measuring near-field and far-field sources are outlined with a calculation of the error committed when considering plane waves radiated from the source.

The concepts of *array pattern*, *resolution* and *maximum side lobe level* of a beamformer are described with a uniform linear array and a regular grid array as the simplest examples of one and two dimensional array geometries. To conclude, the effect of *shading* in a beamformer is presented.

The theoretical information given in this chapter is based on [Johnson and Dudgeon, 1993] and [Brüel&Kjær, 2004].

4.1 Apertures and Arrays

In communication theory, *sensors* are used to convert one energy form into another. In acoustics, the microphones convert acoustic pressure into an electrical signal. Initially they are designed to sample the acoustic field in a certain point of the space no matter the direction of propagation of the acoustic waves, those transducers are said to be *omnidirectional*. It is often useful to focus this transduction in a particular propagation direction, thereby gathering spatial information. An example of this is an *aperture*, which can consist of a continuous sensor of finite dimensions or a combination of spaced sensors.

4.1.1 Finite Continuous Apertures

A continuous aperture function $w(\mathbf{x})$ can be seen as a window through which the wave field is observed. It takes real values from 0 to 1 inside the aperture area and zero outside. It is studied, as the simplest case, in one dimension and its behaviour can be extended to a multidimensional approach.

When a field is observed through a finite aperture, the output is given by:

$$z(\mathbf{x}, t) = w(\mathbf{x}) f(\mathbf{x}, t) \tag{4.1}$$

Where $z(\mathbf{x}, t)$ is the output of the aperture, $f(\mathbf{x}, t)$ is the wave field and $w(\mathbf{x})$ is the continuous aperture function of the sensor. The dual of the convolution theorem implies that windowing in the time domain corresponds to smoothing in the frequency domain. Therefore it can be proved that the spatio-temporal frequency domain version of the output $Z(\mathbf{k}, w)$ is a convolution over wavenumber between the Fourier transform of the field $F(\mathbf{k}, w)$ and the *aperture smoothing function* $W(\mathbf{k})$, being this function:

$$W(\mathbf{k}) = \frac{1}{(2\pi)^3} \int_{-\infty}^{\infty} w(\mathbf{x}) e^{j\mathbf{k}\mathbf{x}} d\mathbf{x} \tag{4.2}$$

Figure 4.1 depicts the most common apertures, namely linear and circular, and their aperture smoothing functions.

Plane Waves Through a Finite Continuous Aperture

Considering a single plane wave propagating in a particular direction $\mathbf{k_0}$ the resulting spectrum $Z(\mathbf{k}, w)$ of the output is

$$Z(\mathbf{k}, w) = S(w) W(\mathbf{k} - \mathbf{k_0}) \tag{4.3}$$

where $S(w)$ is the spectrum of the plane wave. This relation expresses an important concept, when $\mathbf{k}$ equals $\mathbf{k_0}$ the output becomes $Z(\mathbf{k_0}, w) = S(w)W(0)$. For this particular incidence direction $\mathbf{k}$, the output spectrum equals the signal spectrum multiplied by a constant: the value of the aperture smoothing function at the origin. For other values of $\mathbf{k}$ the signal spectrum $S(w)$ is multiplied by a frequency dependent gain $W(\mathbf{k} - \mathbf{k_0})$ that effectively filters the signal. This result can be generalised to the incidence of a superposition of plane waves.

Hence, the sensor is acting here as a *spatial filter* that passes signals propagating from the direction represented by $\mathbf{k_0}$ while rejecting others, considering the main lobe of the smoothing function as the filter passband and the side lobes as the stopband. This

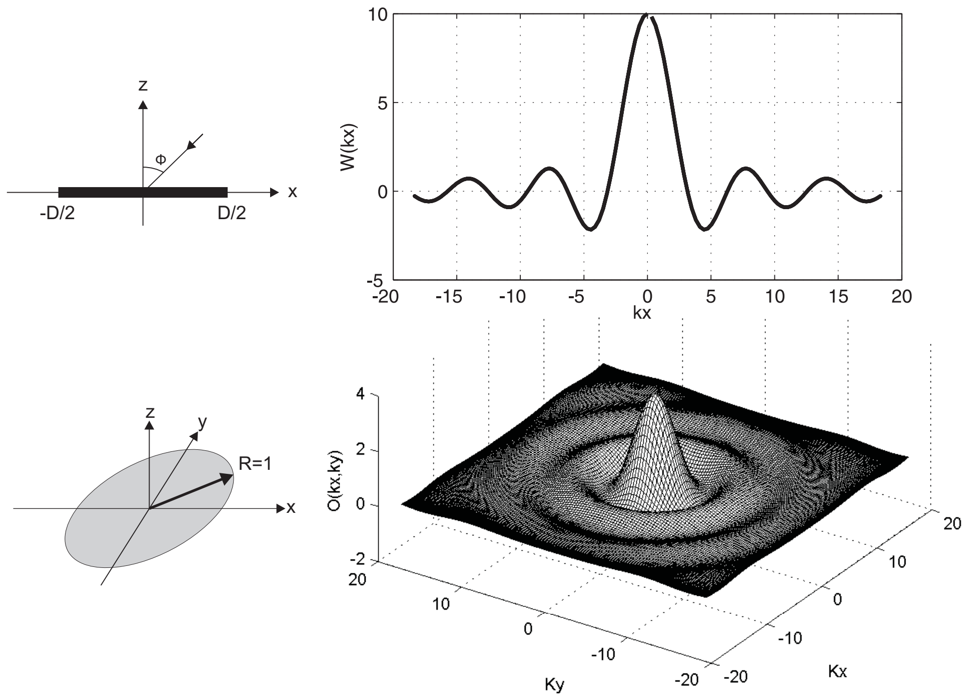

Figure 4.1: Linear and circular apertures on the left and their aperture smoothing function on the right.

represents the aperture directivity characteristic, which can be tuned in order to obtain the optimal directivity pattern for the current purpose.

The main lobe width can be understood as the resolution when separating two directions of propagation, and it directly depends on the spatial extent of the aperture: the larger the extent of the aperture function $w(\mathbf{x})$, the narrower the smoothing function $W(\mathbf{k})$ and the more focused the aperture can be on any specific direction.

Besides, the main lobe of an aperture can be steered to focus on any direction in space, being this the basis of the beamforming theory.

4.1.2 Arrays of Discrete Sensors

A practical way to implement the directivity effects of an aperture in the acoustic field is by means of an array of microphones, which samples the sound field at discrete spatial locations. Microphones can be positioned in both regular or irregular patterns, each gathering its own advantages.

Regular Arrays

A regular grid of microphones is the most straightforward way to produce a sampled array aperture. This approach produces aperture smoothing functions relatively simple to analyse. However, care must be taken in order to prevent from spatial aliasing problems.

Spatial Sampling Aliasing A spatially sampled version of a signal can reconstruct the original signal by means of an interpolation formula under certain conditions (cf. [Johnson and Dudgeon, 1993, p. 77]). The Fourier transform for discrete variables is periodic with period 2π. Hence, in space, the discrete wavenumber variable $\hat{k}$ varies from 0 to 2π or from $-\pi$ to π, as occurring in time for the frequency variable ω. This causes the sampled signal spectrum to equal the sum of replicas of the continuous variable spectrum centred in the periodic spatial frequency $\frac{2\pi}{d}$, being d the spatial sampling interval. Therefore, in order to prevent from overlapping of these replicas, i.e. aliasing, the sampling interval must meet the following expression:

$$d \leq \frac{\pi}{k_{max}} \tag{4.4}$$

where k_{max} is the maximum wavenumber of the spectrum. This is equivalent to say that the sampling interval d must be less than half the minimum wavelength of the signal spectrum. In a multidimensional spatial sampling this condition must be met in all directions, x, y and z.

Once the aliasing is considered and prevented, the output $Z(\mathbf{k}, w)$ from a regular array is the circular convolution between the sampled wave field $Y(\mathbf{k}, w)$ and the aperture smoothing function $W(\mathbf{k})$:

$$Z(\mathbf{k}, w) = \frac{d}{2\pi} \int_{-\pi/d}^{\pi/d} Y(l, w) W(\mathbf{k} - l) dl \tag{4.5}$$

where

$$W(\mathbf{k}) = \sum_{m} w_m e^{j\mathbf{k}md} \tag{4.6}$$

interpreting w_m as the individual weights given to each microphone m, and d as the space between microphones.

The behaviour of the discrete array of microphones can be studied by only analysing $W(\mathbf{k})$. The simplest example is the linear array of equally spaced microphones. Figure 4.2 shows the aperture smoothing function of an array consisting of $M = 50$ microphones separated d distance. It is shown that $W(\mathbf{k})$ is periodic with period $\frac{2\pi}{d}$. Each period of this function consists of a main lobe and a number of side lobes. The height of the main lobe is given by $W(0)$, which equals the number of microphones in a uniform-weight case, 50 in this example. The main lobe width is $4\pi/Md$, therefore, it decreases when increasing the size of the array (either increasing the number of microphones or the space between them) achieving better resolution.

Visible region

It is the range of real angles of incidence (normally between $\pm 90°$) for a given wavelength and constitutes the useful angular region of the array. In one dimension x, the wavenumber value is

$$\mathbf{k}_x = -\frac{2\pi}{\lambda} sin(\phi) \tag{4.7}$$

where ϕ is the angle of incidence. Since $sin(\phi)$ can only take values from -1 to 1, $\mathbf{k}_x$ only takes real values between $\pm\frac{2\pi}{\lambda}$, see figure 4.2. This concept takes importance when designing an array and preventing from grating lobes in this region.

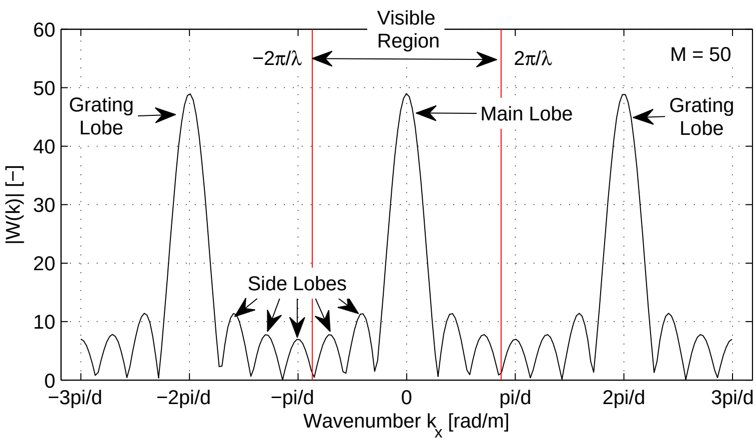

Figure 4.2: The aperture smoothing function magnitude for a fifty-sensor regular linear array. This spectrum has period $\mathbf{k} = 2\pi/d$. The visible region is the part for which $-2\pi/\lambda \leq \mathbf{k}_{0x} \leq 2\pi/\lambda$. Based on [Johnson and Dudgeon, 1993].

Grating Lobes

Grating lobes are false main lobes in the aperture smoothing function, see figure 4.2. They occur at multiples of the period $\frac{2\pi}{d}$ due to the periodicity of $W(\mathbf{k})$, when $\mathbf{k} = \pm\frac{2\pi}{d}$. Therefore, from equation 4.7, they will meet the expression $\pm\frac{2\pi}{d} = -\frac{2\pi}{\lambda} sin(\phi)$, appearing within the visible region at the real angles $sin(\phi) = \frac{\lambda}{d}$, presenting the situations:

- $\lambda < d$, grating lobes occur within the visible region as there are real angles satisfying $sin(\phi) = \frac{\lambda}{d}$. This situation should be avoided.
- $\lambda \approx d$, a grating lobe exists at $\phi = 90°$, when increasing the ratio $\frac{\lambda}{d}$ this lobe decreases until disappearing.
- $\lambda > d$, no grating lobes occur within the visible region as there are not real angles satisfying $sin(\phi) = \frac{\lambda}{d}$.

4.2 Delay-And-Sum Beamforming

Once the operation of apertures and regular discrete arrays is been described, a beamformer can be presented as a discrete array of sensors whose directivity main lobe is focused in a particular direction. One of the applications of a beamformer is producing acoustic images, where the array sensors are omnidirectional microphones working in the audible frequency range.

One technique to steer the directivity of such array of microphones is the so-called *delay-and-sum beamforming*. It consist of applying a different delay to the signal from each microphone of the array, and subsequently add together all the signals, in such a way that a wave propagating in a specific direction in the sound field is added coherently, while waves in other directions add incoherently. Therefore, a maximum of the directivity pattern will be found for that specific direction. Figure 4.3 depicts the concept of the delay-and-sum beamformer.

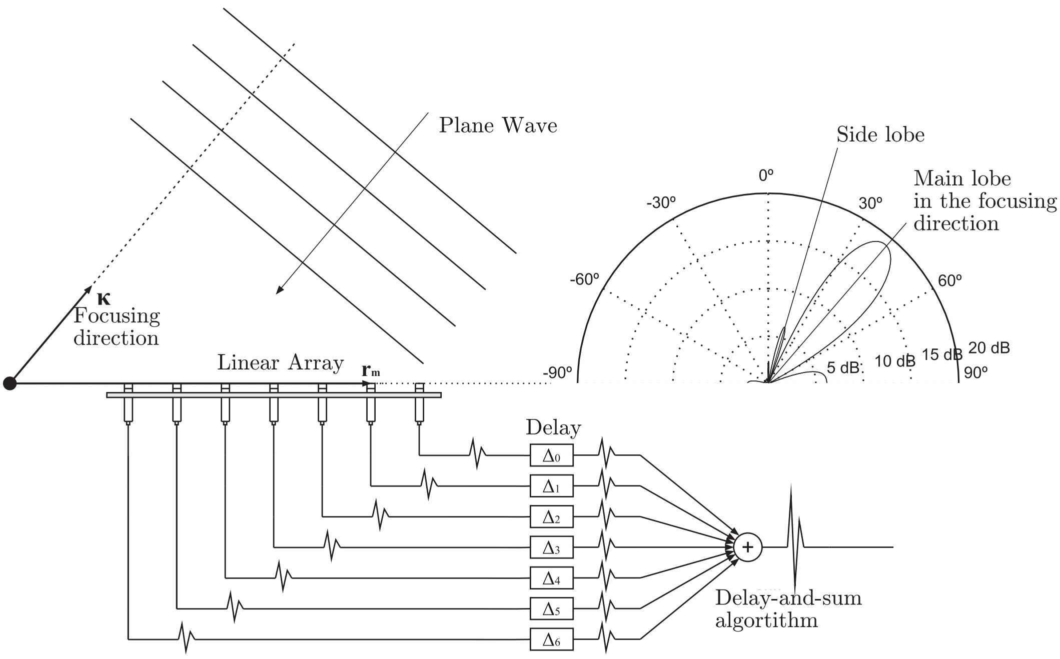

Figure 4.3: In the left part, a linear array focussing in a particular direction κ in the far field. In the right part, its polar directivity pattern with a main lobe in the focusing direction and side lobes in other directions. In the lower part, the delay-and-sum beamforming algorithm is depicted. Based on [Brüel&Kjær, 2004] and [Ginn et al., 2003].

The output of the delay-and-sum beamforming in the time domain is:

$$b(\kappa, t) = \sum_{m=1}^{M} w_m p_m(t - \Delta_m(\kappa)) \tag{4.8}$$

Where κ is a unity vector in the direction in which the array is focused, w_m is a set of weightings applied to the microphone signals, also called *shading* coefficients†, with a value of 1 for a uniform shading. p_m is a pressure signal recorded by each microphone m and $\Delta_m(\kappa)$ is the delay applied to each microphone m when focusing the array in the direction κ.

The Fourier transform of the beamformer output is:

$$B(\kappa, w) = \sum_{m=1}^{M} w_m P_m(w) e^{-jw\Delta_m(\kappa)} \tag{4.9}$$

Where $P_m(w)$ is the Fourier transform of each recorded signal from the m microphones in the array‡.

Beamforming delay values can be calculated in two different ways. In case of a source radiating in the far-field, considering plane waves arriving at the microphones, the beamformer is focused to an infinite point in one direction κ, and delays are calculated without considering the distances from the microphones to the sources:

$$\Delta_m(\kappa) = \frac{\kappa \cdot \mathbf{r_m}}{c} \tag{4.10}$$

where κ is the unity vector in the direction in which the array is focused, $\mathbf{r_m}$ is the position of each m microphone relative to the centre of the array, and c is the speed of sound in the media.

In the case of sources in the near-field, considering spherical waves arriving at the array, the beamformer can be focused to a specific point in the space $\mathbf{r}$, with direction and finite distance to the array, and delays are calculated according to:

$$\Delta_m(\mathbf{r}) = \frac{|\mathbf{r}| - \mathbf{r}_m(\mathbf{r})}{c} \tag{4.11}$$

Where $r_m(\mathbf{r}) = |\mathbf{r} - \mathbf{r}_m|$ is the distance from microphone m to the point in which the array is focused $\mathbf{r}$. In this case the output of the beamformer is function of the vector $\mathbf{r}$ instead of the vector κ. Figure 4.4 depicts such scenario.

†The effect of shading will be described in section 4.7

‡An implicit time factor e^{jwt} is assumed for the frequency domain beamformer output expression.

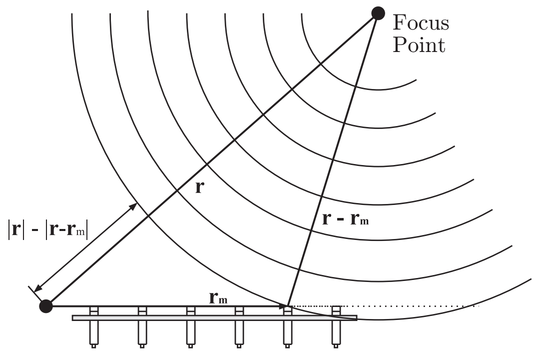

Figure 4.4: Near-field focusing scenario, where waves arriving at the array are considered spherical. Based on [Brüel&Kjær, 2004].

In order to obtain the final acoustic image, a pressure map is calculated by focusing the beamformer in all the possible points within the *mapping plane*. The microphone array is placed at a certain distance z of the object, pressure signals $P_m(w)$ are recorded for a certain time interval. Then the beamforming algorithm is applied to such signals where its main lobe sequentially scan all possible image points, represented by the vector position $\mathbf{r}$, whose direction is κ and comes from a combination of the focusing angles θ_x and θ_y. For each focusing direction, values of pressure are obtained as an output of the algorithm $B(\mathbf{r}, w)$. All these pressure values are gathered and plotted on top of a picture of the source, in this way obtaining an intuitive graph to study the pressure radiation of the structure.

4.3 Near-Field and Far-Field Sources

It has been seen how the calculation of the delays for the beamforming algorithm varies according to whether the sources are located in the near-field or in the far-field (equations 4.10 and 4.11 respectively). In the near-field the wavefront of a propagating wave is perceived curved with respect to the dimensions of the array, whereas in the far-field this wavefront is perceptively plane. In the first case the exact location of the source can be detected, meaning that both incidence direction and distance can be calculated. On the contrary, for plane waves arriving at the array, the exact localization of the far-field sources is difficult since only direction of propagation can be obtained by focusing the beamformer to an infinite distance. A good description of this matter can be found in [Johnson and Dudgeon, 1993]. In case of measuring a three dimensional structure with sources located at different unknown distances from the array, it can be of great interest to obtain these distances besides of their direction of propagation. In a wind turbine scenario, where the sources can be considered to lay in a unique two dimensional plane and where the distance from this plane to the beamformer is known beforehand, it is not necessary to obtain the exact distance of each source to the array. In fact, knowing the sources direction of propagation is enough to localize them by projecting this direction over the wind turbine plane.

In some applications, where the source cannot be assumed to be located in the near-field or far-field, it might be of use to calculate the error induced by assuming far-field (plane waves) instead of near-field (spherical waves) propagation. According to [Johnson and Dudgeon, 1993], this error can be calculated from:

$$\in_m \approx \frac{\mathbf{r}_m}{\mathbf{r}_0} sin\Psi_m \tag{4.12}$$

Where $\in_m$ is error angle committed with Ψ_m denoting the angle between the vectors $\mathbf{r}_m$ and $\mathbf{r}_0$, the first being the position of each microphone m, and the second the vector position of the source, both relative to the centre of the array. Measuring for example, a source 80 m away from an array of 20 m of radius, the maximum error obtained for the most distant sensor is around 14°, meaning that the microphone is actually recording a signal *coming* from a direction with 15° of difference from the focusing direction, therefore the resulting acoustic image will be erroneous.

In case of knowing beforehand the relative distances between the sources and the array, it is recommended to directly use the expression 4.11 instead of expression 4.10, thus this error can be avoided.

4.4 Beamformer Analysis: The Array Pattern

The *array pattern* is used to study the behaviour of a beamformer. From this function, the *radial profile*, the *maximum side lobe level* function and the resolution of the beamformer can be calculated.

Introducing equation 4.10 into equation 4.9, the frequency domain beamformer output can be rewritten as,

$$B(\kappa, w) = \sum_{m=1}^{M} w_m P_m(w) e^{j\mathbf{k}\cdot\mathbf{r}_m} \tag{4.13}$$

Where $\mathbf{k} = -k\kappa$ is the wavenumber vector of a plane wave incident from direction κ, with absolute value being $k = w/c$.

Now the beamformer is focused on direction κ through the choice of the delays $\Delta_m(\kappa)$ applied to each microphone signal. In order to investigate the output of the beamformer for all possible incidence directions, $\mathbf{k}_0$ is defined as the wavenumber vector of a plane wave incident from any direction different from the direction $\mathbf{k}$ the array is focused on, figure 4.5 illustrates such scenario.

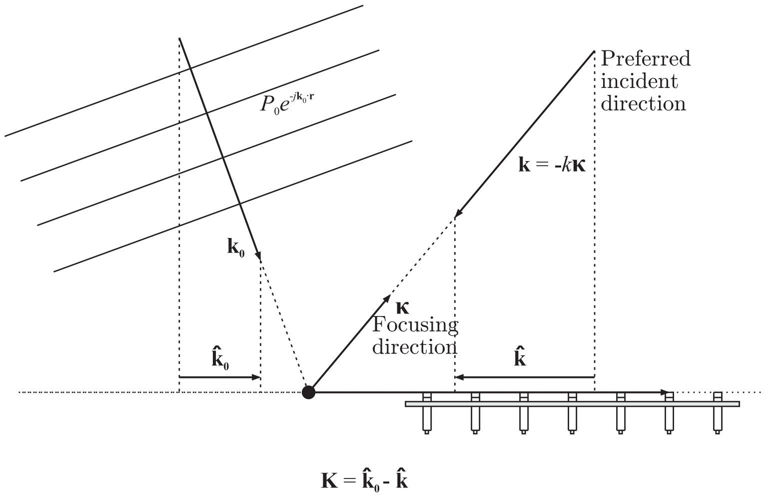

Figure 4.5: An incident plane wave with a wavenumber $\mathbf{k}_0$ different from the preferred wavenumber $\mathbf{k}$. $\mathbf{K}$ is defined as the difference of the projections, $\hat{\mathbf{k}}_0$ and $\hat{\mathbf{k}}$, of the wavenumbers over the plane defined by the array [Brüel&Kjær, 2004].

The pressure measured by the microphones in such a sound field is:

$$P_m(w) = P_0 e^{-j\mathbf{k}_0\cdot\mathbf{r}_m} \tag{4.14}$$

And the output from the far-field beamformer leads to:

$$B(\kappa, w) = P_0 \sum_{m=1}^{M} w_m e^{j(\mathbf{k}-\mathbf{k}_0)\cdot\mathbf{r}_m} \equiv P_0 W(\mathbf{k}-\mathbf{k}_0) \tag{4.15}$$

Where the far-field array pattern is defined as

$$W(\mathbf{K}) \equiv \sum_{m=1}^{M} w_m e^{j(\mathbf{K})\cdot\mathbf{r}_m} \tag{4.16}$$

being $\mathbf{K} = \mathbf{k} - \mathbf{k}_0$ the difference of the projections of $\mathbf{k}$ and $\mathbf{k}_0$ over the plane defined by the array. The array pattern is the analogous of the aperture smoothing function described in section 4.1, given by equation 4.2 for continuous apertures, and it represents the same concept of *spatial filtering* where only waves propagating in a particular direction pass while others are rejected. The array pattern, in case of a uniform shading, i.e. $w_m = 1$, depends only on the geometry of the array and it is often normalized dividing it by the number of microphones W/M. The effect of non-uniform shading is discussed in section 4.7.

It is important to point out that the expression of the array pattern for a beamformer in the near-field differs from the far-field expression shown previously. This is due to the fact that the delays calculation and the pressure in each microphone differs from far-field to near-field scenarios. Figure 4.6 shows an incident spherical wave in near-field, where the pressure at each microphone position is:

$$P_m(w) = \frac{P_0}{|\mathbf{r}_0 - \mathbf{r}_m|} e^{-j\frac{w}{c}|\mathbf{r}_0 - \mathbf{r}_m|} \tag{4.17}$$

where $\mathbf{r}_0$ is the position vector of an arbitrary source and $\mathbf{r}_m$ is the position vector of each microphone m of the array.

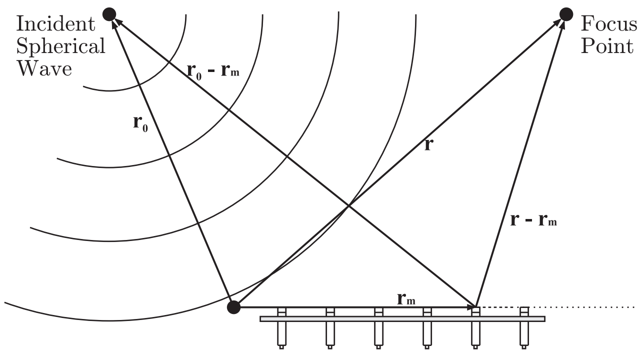

Figure 4.6: An incident spherical wave arriving from a source placed at point $\mathbf{r}_0$ different from the focusing point $\mathbf{r}$.

The beamformer output is rewritten by introducing equations 4.11 and 4.17, leading to:

$$B(\mathbf{r}, \mathbf{r}_0, w) = P_0 \sum_{m=1}^{M} w_m \frac{1}{|\mathbf{r}_0 - \mathbf{r}_m|} e^{-j\frac{w}{c}[|\mathbf{r}| - |\mathbf{r} - \mathbf{r}_m| + |\mathbf{r}_0 - \mathbf{r}_m|]} \tag{4.18}$$

where the position vectors $\mathbf{r}_0$, $\mathbf{r}_m$ and $\mathbf{r}$ are depicted in figure 4.6.

Then, the near-field array pattern for a finite distance is:

$$W(\mathbf{r}, \mathbf{r}_0, w) = \sum_{m=1}^{M} w_m \frac{1}{|\mathbf{r}_0 - \mathbf{r}_m|} e^{-j\frac{w}{c}[|\mathbf{r}| - |\mathbf{r} - \mathbf{r}_m| + |\mathbf{r}_0 - \mathbf{r}_m|]} \tag{4.19}$$

Expressions 4.16 and 4.19, both for the array pattern in both near-field and far-field are very similar, only differing in two facts. First, the inclusion of a term $\frac{1}{|\mathbf{r}_0 - \mathbf{r}_m|}$, which models the spheric divergence of the propagating acoustic pressure in near-field; and second, the fact that the array pattern is now a function of two position vectors $\mathbf{r}_0$, $\mathbf{r}$, and frequency w.

It can be seen in the next section that obtaining an array pattern as a function of the difference vector **K**, as being the case for far-field, simplifies to a high extent the analysis of a beamformer, since a single function contains information of the outcome of the beamformer for all frequencies and focusing angles. On the contrary, an array pattern as a function of the three mentioned variables complicates the analysis since all frequencies and focusing points should be analysed one by one, becoming a tedious and impractical approach.

The behaviour of an array geometry can be easily understood from the far-field calculations. Thus, it is decided for simplicity to perform the theoretical study assuming plane waves arriving at the array.

4.4.1 The Linear Array

A linear array of microphones is the simplest example of a beamformer, where the wavenumber difference vector **K** is defined for one dimension. The array pattern can be presented as a function of $\mathbf{k}_0$ and the angle of incidence ϕ_i as it can be seen in figure 4.7. Being the array pattern figure different for each frequency and focus direction.

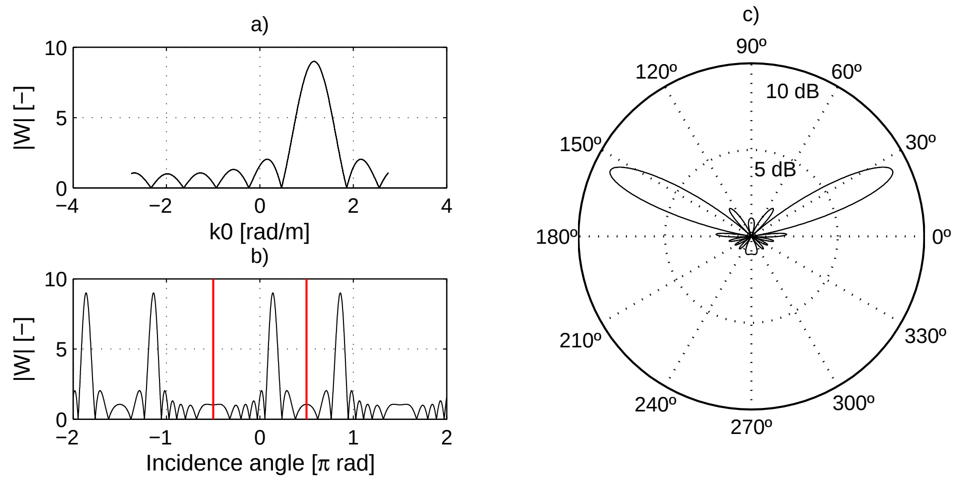

Figure 4.7: (a) The array pattern of a uniform linear array of 9 microphones spaced 1 m as a function of the incident wavenumber $\mathbf{k}_0$. It is focused 40° off axis and studied at 150 Hz. (b) The same array pattern as a function of the incident angle, red lines represent the visible angular range ±90°. (c) The polar directivity pattern of such array.

However, it is of great advantage to study the array pattern as a function of **K**, since it contains information for all focus directions and frequencies. Figure 4.8 shows the same array pattern of figure 4.7 as a function of **K**.

Active Part According to [Brüel&Kjær, 2004], it is defined as the maximum useful **K** for a certain scenario. It is given for the maximum difference of the wavenumber vectors

$\mathbf{K}_{max} = |\mathbf{k} - \mathbf{k}_0|$ evaluated at the maximum frequency of interest. This difference is maximum for the largest opening angle of the array θ_{max} and the largest angle of a possible incoming wave ϕ_{max}. If the range of possible directions of an incoming wave is known beforehand, i.e. ϕ_{max} is known, the active part of the array is given by:

$$K^{\theta}_{max}(w_{max}) = [sin(\phi_{max}) + sin(\theta_{max})]\frac{w_{max}}{c} \tag{4.20}$$

In case the range of possible directions of incoming waves is not known, ϕ_{max} is assumed to be 90°, and the previous expression becomes:

$$K^{\theta}_{max}(w_{max}) = [1 + sin(\theta_{max})]\frac{w}{c} \tag{4.21}$$

Then the active part when studying an array pattern lies within the range $|\mathbf{K}| \leq K^{\theta}_{max}(w_{max})$ depicted by red lines in figure 4.8 for w_{max}= 200 Hz, $\theta_{max} = 30°$ and $\phi_{max} = 90°$.

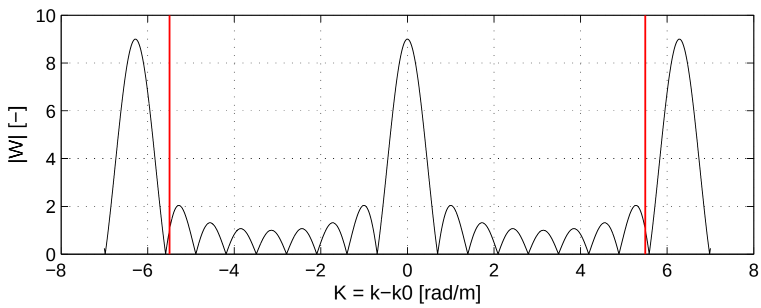

Figure 4.8: The array pattern of a linear array as a function of the wavenumber difference **K**. All the information for all focus directions and all frequencies is contained. Red lines depict the limits of the active part of the array pattern for $w_{max} = 200$ Hz, $\theta_{max} = 30°$ and $\phi_{max} = 90°$.

The Planar Array

The array pattern of a two dimensional beamformer consists of a three dimensional figure, with different wavenumber difference vectors ($\mathbf{K}_x$ and $\mathbf{K}_y$) for each dimension of the array plane. Figure 4.9 shows an example of the array pattern of a two dimensional beamformer with a grid geometry consisting of 45 microphones.

However, with a view in further calculations, it is more practical to study the array pattern of planar arrays in each direction separately, as depicted in figure 4.10.

The array pattern contains all the information of the beamformer. However, further calculations may be performed to better illustrate certain characteristics of the array, such as resolution and useful dynamic and frequency ranges.

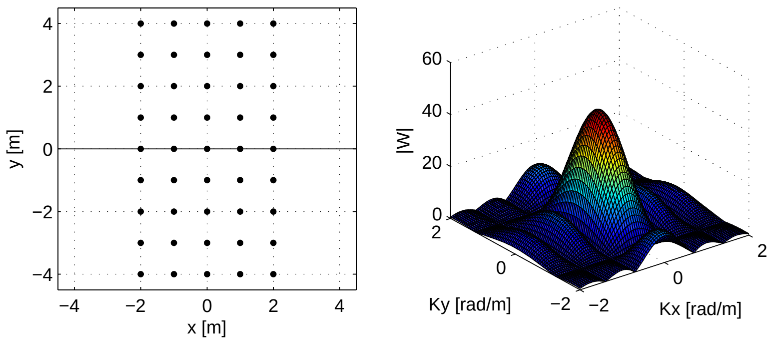

Figure 4.9: A grid array geometry with 45 microphones of 4x8 m and its corresponding array pattern in three dimensions.

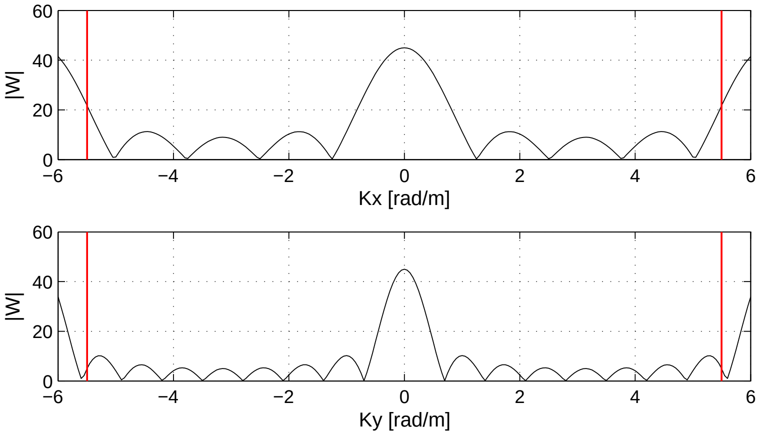

Figure 4.10: Array pattern of a regular grid array of 4x8 m with 45 microphones depicted in directions x and y separately. Red lines depict the limits of the active part of the array pattern for $w_{max} = 200$ Hz and $\theta_{max} = 30°$.

4.5 Beamformer Analysis: The Resolution

The resolution can be understood as the ability of the beamformer to separate two plane waves arriving in slightly different directions. This definition is given in [Brüel&Kjær, 2004], and ideally, it is consistent with the Rayleigh criterion which states that two waves arriving with different directions of propagation, defined by $\mathbf{k}_1$ and $\mathbf{k}_2$, are resolved when the peak of a shifted array pattern $W(\mathbf{k}-\mathbf{k}_2)$ falls on the first zero of the other $W(\mathbf{k}-\mathbf{k}_1)$. Therefore, the minimum difference between $\mathbf{k}_1$ and $\mathbf{k}_2$ satisfying this criterion, leads to the resolution in terms of wavenumber, denoted R_K.

Main Lobe Width The value of R_K is considered the main lobe width and, according to [Johnson and Dudgeon, 1993], different methods for its calculation exist:

- **Peak-to-zero**: it is the wavenumber difference from the peak of the main lobe and the first zero encountered in one direction.
- **Full-Width Half-Maximum (FWHM)**: it is the full width of the main lobe at one-half the peak value measured in terms of wavenumber. It can be applied to the squared magnitude of the array pattern.
- **Parabolic width**: it is measured from the FWHM of a parabola fitted to the main lobe of the normalized array pattern. According to the literature, this method suits best for asymmetric array patterns and those that do not have conveniently located zeros.

It is important to note that none of them provides the same value of R_K which in any case is proportional to the aperture size D. Besides, as it is shown in [Johnson and Dudgeon, 1993], for regular arrays, they differ only by a constant of proportionality, as it is shown in table 4.1.

Main Lobe Width Calculation Method	Value
Peak To Zero Distance	$2A$
FWHM	$2.4A$
FWHM squared	$1.77A$
Parabolic Width	$2.2A$

Table 4.1: Different calculation methods of the array pattern main lobe width for regular arrays and their proportional outcomes.

Due to their relationship, it seems that any of these measures is valid. Nevertheless, for irregular arrays their outcomes are no longer related by those constants, as the main lobe might be non-symmetric or present other irregularities. Therefore care must be taken when deciding a method for the resolution calculation, which must be consistent for different array geometries in a certain real scenario.

Once the wavenumber main lobe width R_K is obtained, the resolution can be calculated in terms of the minimum distance between two sources such that they can be resolved. This more practical number can be obtained geometrically for sources at a finite distance, and it is given by:

$$R(\theta) = \frac{zR_K}{k}\frac{1}{cos^3\theta} \tag{4.22}$$

Where k is the absolute wavenumber, θ is the focusing angle and z is the measurement distance for the actual focusing point in the mapping plane. According to this equation, the resolution value increases when increasing the measurement distance, meaning that two waves are more difficult to separate when measuring at larger distances. It also increases when increasing the focusing angle θ,

$$R(\theta) = \frac{R_{axis}}{cos^3\theta} \tag{4.23}$$

getting more than 50% greater for an opening angle of 30°. This opening angle is often considered as a limit when defining the measurement distance and the mapping area of an acoustic image. Figure 4.11 shows the ratio between off-axis and on-axis resolution.

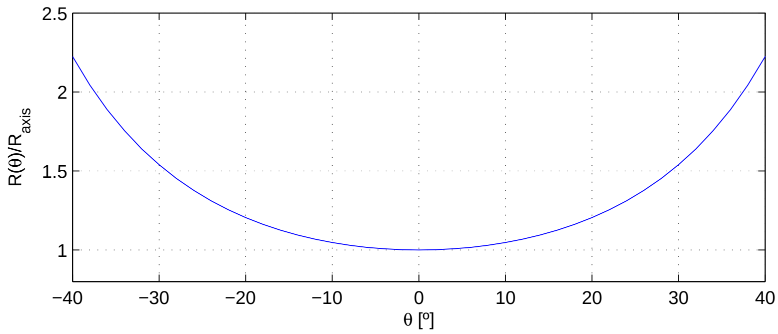

Figure 4.11: The ratio between off-axis and on-axis resolution. Note that resolution increases a 50% for an opening angle of 30°

4.6 Beamformer Analysis: Maximum Side Lobe Level

The level of the side lobes in the array pattern determines the dynamic range of a beamformer. The side lobes cause waves propagating in directions different from the focus direction κ to be added in the measurement of the main lobe direction, thereby creating false images in the final pressure map. Hence, the difference between the main lobe level and the maximum side lobe level (MSL) constitutes the effective dynamic range of the system. Levels below this range cannot be ascribed to waves propagating in the focus direction, thus their information is meaningless for the acoustic image.

From the MSL function it is possible to analyse the maximum side lobe levels of a beamformer for all frequencies and focus angles as a function of K. Prior to its calculation, the *radial profile* W_p of an array pattern is defined as

$$W_p(K) = 10\log_{10}\left[\max_{|\mathbf{K}|=K} |W(\mathbf{K})|^2 / M^2\right] \tag{4.24}$$

where K is the absolute value of the wavenumber difference vector $\mathbf{K}$ and M is the number of microphones in the array. It consists of the maximum values of the array pattern in dB as a function of $K = |\mathbf{K}|$. Figure 4.12 shows the radial profile of an array with a random distribution of microphones in a circular aperture.

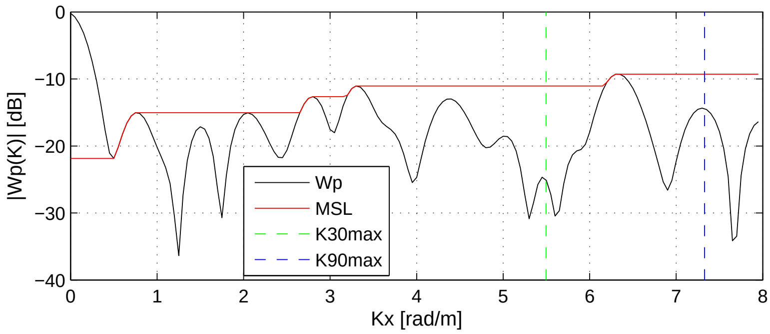

Figure 4.12: Radial profile and MLS functions from a random array with 45 microphones within a circular aperture of 20 m. Limit values for K are depicted for a highest frequency of 200 Hz and maximum opening angles of 30° and 90°.

From the radial profile, the MSL function is calculated as

$$MSL(K) = \max_{K^0_{min} < K' \leq K} W_p(K') \tag{4.25}$$

which consists of the peak value of the radial profile when increasing K from the first minimum K^0_{min} up to the highest wavenumber of interest, $K^{30°}_{max}$ for a maximum opening angle of 30° or $K^{90°}_{max}$ for 90°. Figure 4.12 shows the MSL function. It increases with K, thus the effective dynamic range of the beamformer is the MSL value at the highest K within the active part, i.e. the value of K for the considered highest frequency and opening angle.

4.7 Shading Coefficients

It has been stated in section 4.4 that the array array pattern depends only on the geometry of the array of microphones. This is true in case of a uniform shading, i.e. all the shading coefficients w_m being equal to 1. The shading coefficients are weights given for each microphone signal prior to their addition in the delay-and-sum beamforming algorithm.

Giving different values to such coefficients can modify the array pattern. For instance, it is possible to set the coefficients in order to obtain a Hamming windowing shading, obtaining a much better side lobe suppression at the cost of resolution [Brüel&Kjær, 2004].

4.8 Summary

The most relevant issues of the beamforming theory have been described throughout this chapter. An introductory section about apertures and their operation has been included describing important concepts for the understanding of a beamformer, such as the aperture smoothing function and its spatial filtering effect, the spatial aliasing in discrete apertures, the visible region of an aperture and the effect of the grating lobes.

The delay-and-sum beamforming concept has been explained next with emphasis in the calculation of the delays for the algorithm and a discussion about when to consider sources in the near-field or in the far-field. It has been shown how the calculation of the delays for spherical waves in the near-field brings better results avoiding a possible error committed when considering plane waves.

A group of functions and calculations have been presented for the analysis of a beamformer. The array pattern and its interpretation as a function of the wavenumber difference vector $\mathbf{K}$ serves as a starting point for the calculation of the resolution and dynamic range of the beamformer. The maximum side lobe level (MSL) function provides a measure of the dynamic range of the system, limited by the level difference between the main lobe and the side lobes that can cause false images in the final acoustic image. Those calculations have been described assuming plane waves arriving at the array in a far-field scenario, the array pattern for near-field has also been presented, where waves arriving at the array are considered spherical. In that case, the array pattern is a function of three variables, leading to a more complex study

Finally, the effect of the *shading* coefficients have been described. It is possible to lower the side lobe level at the cost of a poorer resolution, effect that might help for expanding the dynamic range in the higher frequencies.

The proper understanding of all of these concepts is crucial for the design of an optimal beamformer, where the geometry of an array defines the dynamic range and the resolution as a function of frequency. Both have to be evaluated carefully to achieve the optimal solution for a specific application, meaning by the optimal, an array meeting the required performance using the smallest dimensions and the lower number of microphones.

Chapter 5

Specifications

This chapter presents the specifications of the wind turbine and the most important geometrical considerations of the set-up.

5.1 Wind Turbine Specifications

The dimensions of the wind turbine used as an example of a large structure are presented in the following subsections.

5.1.1 Wind Turbine Dimensions

A wind turbine can be considered large when it provides more than 1500 kW [Wind Power Database, 2009]. In that case, its rotor diameter typically ranges from 60 to 130 m, while the tower height ranges from 70 to 160 m. The rotor diameter, tower height and blades and nacelle sizes of the selected turbine are included in table 5.1.

5.1.2 Frequency Range of Interest

In 2008, the Danish company Delta carried out a project focused on the determination of low frequency noise from large wind turbines. This project is divided into a series of reports. One of these reports presents the sound power of three different large wind turbines, measured according to IEC 61400-11:2002. [Delta, 2008]. Wind turbines from 2300 kW to 3600 kW are analysed. Their rotor diameters range from 80 to 107 m and their tower sizes from 60 to 100 m. The power and the dimensions of the selected wind turbine lie within these ranges.

Description	Size [m]
Rotor diameter	90
Tower height	80
Top diameter of the tower	2
Bottom diameter of the tower	4
Blade length	44
Blade base width	3.5
Blade tip	0.3
Nacelle length	13
Nacelle height	4
Nacelle width	3.5
Total height	125
Maximum width	90

Table 5.1: Dimensions of the selected as a representative large wind turbine.

From the analysis of this report, it can be seen that there exist prominent tonal components below 200 Hz, which are believed to be due to the rotational character of the gear. Besides, there is a distinct tone at around 40 Hz. Thus, the frequency range of interest is set up from 40 to 200 Hz. Figure 5.1 shows an A-weighted FFT-spectra of the noise of four different turbines, working in different modes. This figure is directly extracted from [Delta, 2008].

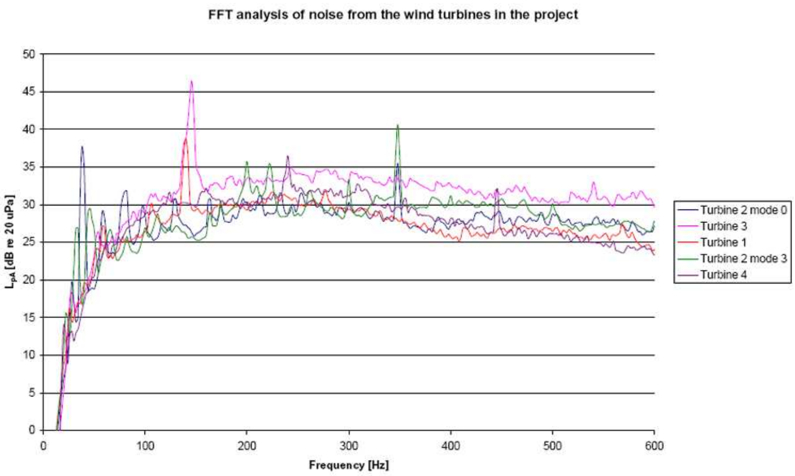

Figure 5.1: A-weighted FFT-spectra of the four the wind turbines in Delta's report [Delta, 2008].

It is important to mention that the tonal distribution and audibility of a wind turbine noise profile is altered depending on the wind speed. Since the wind turbine operates at variable rotational conditions according to the wind speed, different resonances of the mechanical parts can be excited.

5.2 Definitions

For a clear understanding of the following sections, these definitions are given:

- Mapping area size: It is the size of the area to be scanned by the beamformer and resulting size of the acoustic image.
- Wind turbine area of interest L_H x L_V: It is the area of the wind turbine to be analysed. It should cover, at least, the whole rotor and part of the tower of say, 20 m.
- Focusing point: It is the point the array is focusing at.
- Measurement distance z: It is the distance between the array and the focusing point.
- Horizontal measurement distance z_H: It is the distance between the tower and the array centre.
- Array centre height h_{array}: It is the distance from the ground to the centre of the array.
- On-axis pointing height h_{axis}: It is the height of the focus point when focusing the array on-axis in both directions x and y.

Figure 5.2 shows these definitions.

5.3 Requirements

Mapping Area Size

The mapping area size should cover, at least, the whole area of interest of the wind turbine. Then, the area of interest is set to $L_H = 90$ m and $L_V = 110$ m. A margin of 5 m is left in the borders of such area, defining that way the mapping area size.

Resolution

According to [Oerlemans and López, 2005], the noise radiated by a medium-large wind turbine is mostly produced by the outer part of the blades (*not the very tip*) and a minor contribution of the rotor hub. The wind turbine blade in this case is 44 m, thus an hypothetical source located in its outer part could be placed around 40 m from the hub. Moreover, it is known that there is a possible noise source caused by the interaction between the blade and the tower.

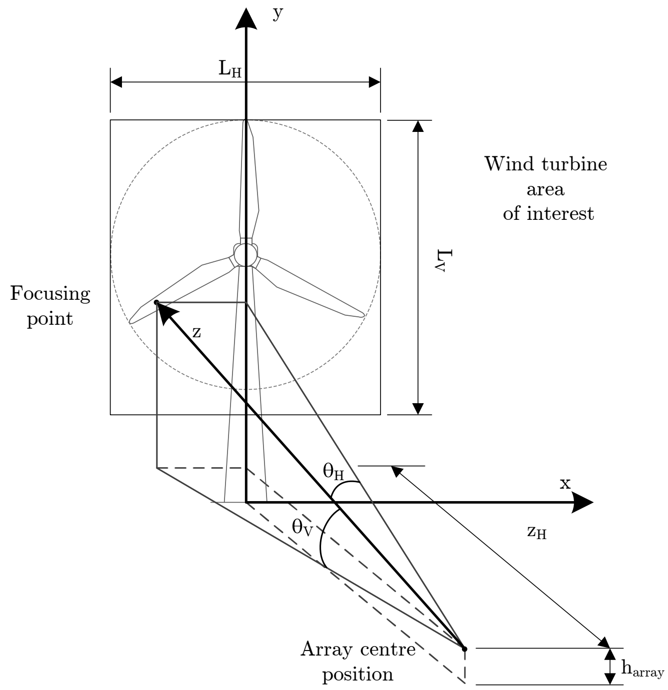

Figure 5.2: Measurement distance z, horizontal measurement distance z_H, opening angles θ_H and θ_V, focusing point and wind turbine area of interest representation.

The resolution is required to be such that it is possible resolve, at least, two monopole sources placed 40 m far from each other. In that way, it is possible to identify hypothetical sources located at the blades, rotor hub and tower.

Dynamic Range

The dynamic range of the system is defined by its MSL (cf. chapter 4). The MSL for a practical application is suggested to be less than -10 dB at f_{max} [Brüel&Kjær, 2004]. Nevertheless, it must be mentioned that the MSL number is not equivalent to the dynamic range of the system. It could be equal in a single source scenario, however, when multiple sources are present, the side lobes of the beamformer scanning different directions overlap and cause a decrease in the overall dynamic range of the acoustic image. Thus the dynamic range varies for different source scenarios and cannot be predicted. Therefore, the requirement is set for the MSL to be less than -10 dB, being aware that the dynamic range is not represented by this number, but depends on it.

5.4 Geometrical Considerations

A discussion about some important practical aspects of the set-up, such as where the array should be positioned, its on-axis pointing height or the mapping area size is presented in this section.

5.4.1 Array Centre Height

The array size D can be theoretically estimated using the following expression,

$$D = \frac{a}{R} \frac{z}{\cos^3(\theta)} \lambda \tag{5.1}$$

where a is $a \approx 1.22$ for continuous circular apertures, R is the resolution, θ is the off-axis angle, z is the measurement distance and λ is the wavelength [Brüel&Kjær, 2004].

In order to fulfil the resolution requirement at the lowest frequency and in the worst situation of z and θ, array sizes of at least 40 m are needed. This value is worked out from equation 5.1, considering $R = 40$ m and $\lambda = c/f = 343/40$ m. The worst cases of z and θ are estimated considering the array placed 80 m away from the turbine and covering the whole area of interest. For this measurement distance the resulting opening angle θ_V is 35° approximately. Thus,

$$D = \frac{1.22}{40} \frac{80}{\cos^3(35°)} \frac{343}{40} \approx 40 \text{ m}$$

The array is not placed totally parallel to the wind turbine, but leant. Neither the on-axis pointing direction nor the exact size of the array can be exactly defined beforehand, thus an array centre height of 15 m is considered as an initial approximation.

5.4.2 Measurement Distance

Before discussing the selection of the horizontal measurement distance z_H, it is important to recall from chapter 4, that the resolution directly depends on the measurement distance z, while it inversely does on the opening angle θ according to equation,

$$R(\theta) = z \frac{R_K}{k} \frac{1}{\cos^3(\theta)} \tag{5.2}$$

In order to understand the influence of the measurement distance and the opening angle on the resolution, two examples are presented: one with the array close to the structure and the other far from it.

Example 1: Array close to the wind turbine As it can be seen in figure 5.3 (green lines), placing the array close to the wind turbine involves that:

- The horizontal measurement distance z_H decreases.
- The maximum opening angle θ increases.
- The measurement distance z also decreases, but it subtancialy varies depending on the focusing point.

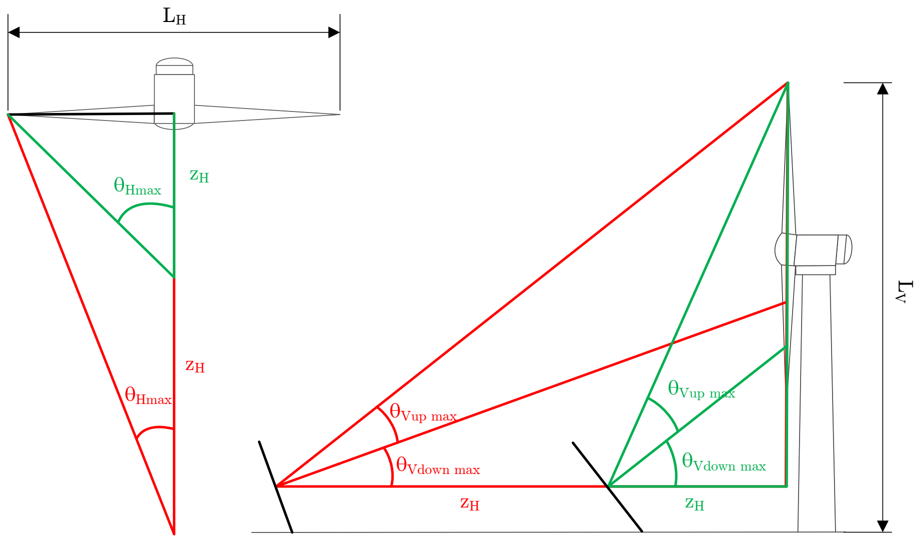

Figure 5.3: Distances and opening angles for the two examples: array close to the wind turbine (green) and array far from the wind turbine (red).

This implies the following advantages and disadvantages:

- *Advantage*: There is an improvement in the overall resolution, due to the decrease of the measurement distance for all the focusing points.
- *Disadvantages:* The off-axis resolution is worsen due to the increase of the opening angle. This effect is more prominent in mapping positions where z becomes maximum. Hence, there is a loss in the homogeneity of the resolution along the mapping area caused by the non-uniform values of z.

Example 2: Array far from the wind turbine As it can be seen from figure 5.3 (red lines), placing the array far from the wind turbine involves that:

- The horizontal measurement distance z_H increases.

- The maximum opening angle θ decreases.
- The difference between the maximum and minimum measurement distance decreases.

This implies the following advantages and disadvantages:

- *Advantage*: The resolution is more homogeneously distributed than in the previous example, since z does not vary that much with the mapping position and the maximum opening angle is smaller.
- *Disadvantages*: The increase of z_H implies a worsen in the resolution.

Figure 5.4 depicts both examples for a grid array of 40 m, 200 microphones at 40 Hz, in 5.4.a z_H is 80 m, while in 5.4.b z_H is 125 m, which is the horizontal measurement distance suggested in [IEC 61400-11:2002, 2003]†. These plots show the resolution in the y-axis of the wind turbine. It can be seen that when the array is closer to the wind turbine (figure 5.4a), the overall resolution improves. Nevertheless, the expected lack of homogeneity is manifested as the measurement distance z increases. Thus, the extremes of the mapping area would have very different spatial resolution, which is undesired. Figure 5.4b shows that the resolution is worsened, however its values are more uniform than in the previous example.

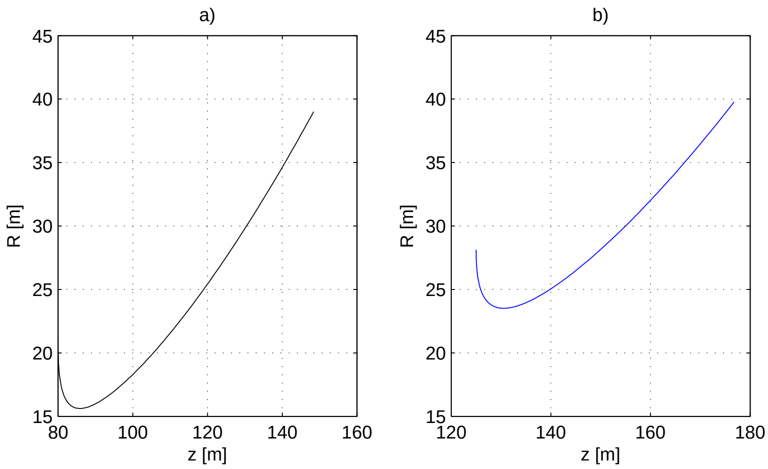

Figure 5.4: Resolution in the y-axis over measurement distance z for a grid array of 40 m, 200 microphones at 40 Hz. Both plots show the influence of the horizontal measurement distance z_H in the resolution. a) z_H is set to 80 m. b) z_H is set to 160 m.

†According to the IEC 61400-11:2002, the required downwind horizontal measurement distance is given by $R_0 = H + \frac{D}{2}$, being H the distance from the ground to the rotor centre and D the rotor diameter. This distance is just used as a reference, since this ICE is referred to noise emission assessment, not to noise source identification.

As it is shown in both examples, the selection of z_H constitutes a difficult compromise between fine resolution and homogeneity distribution of it.

5.4.3 On-axis Pointing Height

In the previous examples, the arrays are pointing to a height such that $\theta_{V\ down}$ equals $\theta_{V\ up}$. As both opening angles are the same, the worst scenario occurs when z is maximum, i.e. when the array is focusing at upper parts of the mapping area. In order to compensate for the increase in z, $\theta_{V\ up}$ can be reduced. This can be achieved focusing the array to a higher point, or equivalently changing the inclination of the array (figure 5.5a). The resulting resolution, when z_H is 80 m and h_{axis} is 75 m, is depicted in figure 5.6a for a grid array of 40 m, 200 microphones at 40 Hz.

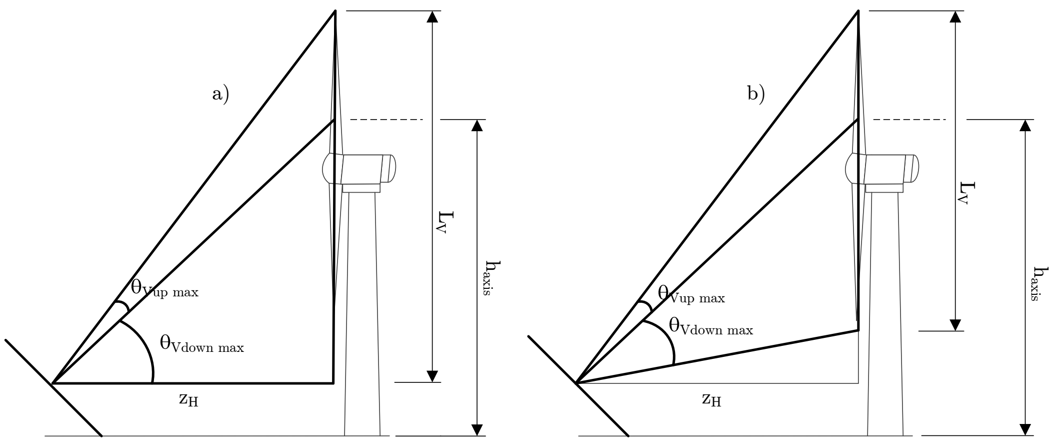

Figure 5.5: Elevation sketch of the wind turbine. a) The on-axis pointing height is increased. Thus, $\theta_{V\ up}$ decreases, compensating for the loss of resolution caused by the increase of z in the upper parts of the mapping area. b) The mapping area is reduced so that $\theta_{V\ down}$ can be minimised and an optimization of the resolution in terms of homogeneity can be achieved.

Besides, since it is not necessary to map the whole tower of the wind turbine, the mapping area size can be reduced. This situation is depicted in figure 5.5b. In that way, $\theta_{V\ down}$ decreases, leading to an optimization of the resolution. The resolution resulting from this situation is shown in figure 5.6b.

From the comparison of the resolution in the previous cases and in order to meet the requirements, it seems convenient to:

- Reach a compromise in the selection of z_H to obtain a fine resolution.
- Adjust h_{axis} in order to obtain an homogeneous resolution within the whole area of interest.

The resolution for several combinations of z_H and h_{axis} has been estimated. Setting them to 80 and 75 m respectively, leads to a proper trade-off of homogeneity and quality.

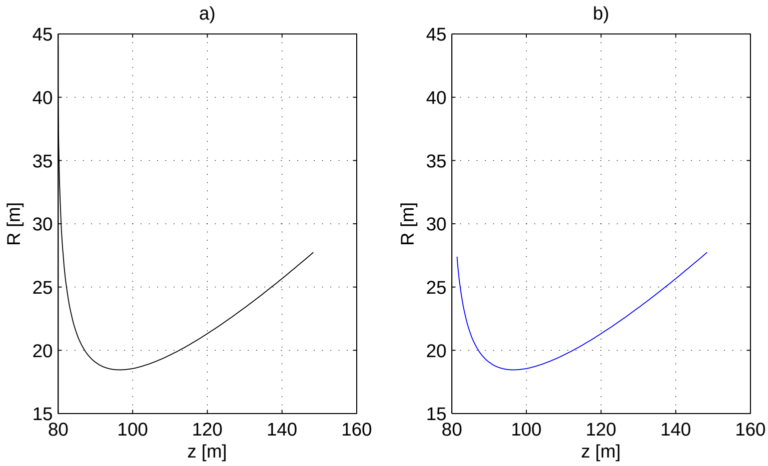

Figure 5.6: Resolution in the y-axis over measurement distance z for a grid array of 40 m, 200 microphones at 40 Hz. a) Influence of the on-axis pointing height in the resolution. b) Influence of the mapping area optimization in the resolution.

This geometry configuration results in a maximum horizontal opening angle $\theta_{H\ max}$ of 29°, and maximum vertical opening angles of $\theta_{Vdown\ max}$ and $\theta_{Vup\ max}$ of 36° and 17° respectively. The eventual geometrical specifications are depicted in figure 5.7.

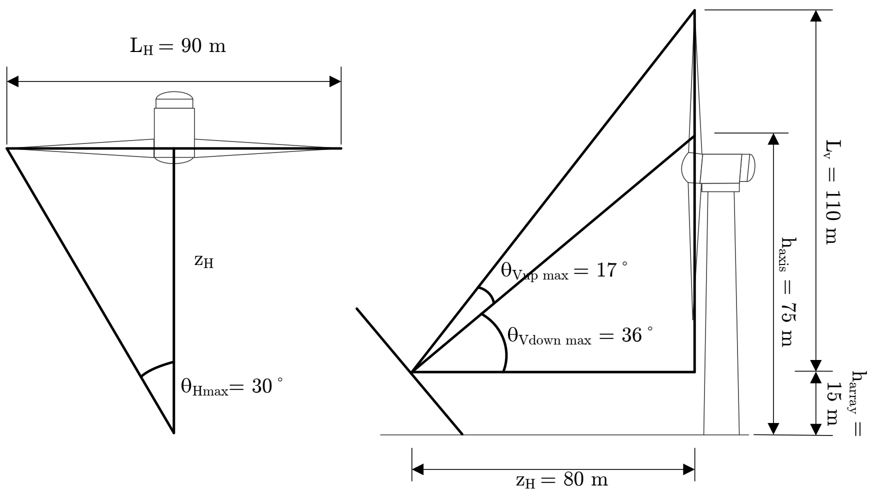

Figure 5.7: Illustration of the eventual set-up specifications.

5.5 Definition of the Sound Field

According to section 4.3, it is important to define whether the sources are located in the near or the far field, since this determines the behaviour of the beamformer and the calculation of the delays for the delay-and-sum algorithm.

The array horizontal distance to the wind turbine causes measurement distances range from 80 to 136 m at the highest point. The array aperture size is estimated to be 40 m, thus an estimation of the induced error of assuming plane waves arriving at the array can be calculated from equation 4.12. Introducing approximated values of 110 m for the source distance and 20 m for the most distant microphone, both relative to the centre of the array, leads and error of:

$$\in_m \approx \frac{\mathbf{r}_m}{\mathbf{r}_0} sin(\pi/2) = \frac{20}{110} sin(\pi/2) \equiv 10.5^\circ \tag{5.3}$$

Which is considered a large error that indicates that waves arriving at the array are spherical. Hence, the calculation of the delays of the beamforming algorithm must be performed according to equation 4.11 for finite focusing distances.

5.6 Summary

In this chapter, the specifications of the wind turbine under study has been described, including dimensions and frequency range of interest. Besides, a discussion about the most suitable position of the array regarding the resolution requirement has been given. The centre was decided to be placed 80 m away from the turbine, and 20 m from the ground in an upwind position. The array on-axis direction points to a height of 75 m. This height was chosen so that the ratio between measurement distance and opening angle guaranteed an homogeneous spatial resolution even in the farthest focusing points.

All these specifications are summarized in table 5.2 and are depicted in figure 5.7.

Description	Parameter	Value
Wind turbine specifications		
Rotor diameter	RD	90 m
Tower height	TH	80 m
Total height	H_{Total}	125 m
Maximum width	W_{Total}	90 m
Maximum frequency	f_{max}	200 Hz
Minimum frequency	f_{min}	40 Hz
Array position		
Horizontal meas. distance	z_H	80 m
Array center height	h_{array}	15 m
On-axis pointing height	h_{axis}	75 m
Max. horizontal off-axis angle	$\theta_{H\ max}$	23°
Max. vertical off-axis angle	$\theta_{Vdown\ max}$	36°
Max. vertical off-axis angle	$\theta_{Vup\ max}$	17°
Design requirements		
Mapping area size		100x120 m
Wind turbine area of interest	L_HxL_V	90x110 m
MSL	T or DR	-10 dB
Spatial resolution	R	40 m

Table 5.2: Specifications summary.

Chapter 6

Array Design

This chapter describes an approach to the design of a beamformer able to localize the noise sources of the wind turbine in the scenario portrayed in chapter 5.

The design process is based on finding the optimum parameters (typically the number of microphones and aperture size) for all the geometries under study. Hence, an acoustic image simulation tool is developed to ease this task. Certain design criteria are fixed, so that a more systematic procedure can be followed.

6.1 Acoustic Image Simulation

The characteristics of a beamformer, in terms of resolution and dynamic range, can be inferred:

- Theoretically: through the study of its array pattern, whose main lobe width can be measured to obtain an estimation of the resolution; and the analysis of the MSL function, in order to obtain an idea of the dynamic range of the array.
- Empirically: through the inspection of an acoustic image resulting from a simulation of the beamformer in a virtual scenario.

The theoretical tools for the analysis of a beamformer have been described in sections 4.4, 4.5 and 4.6. In order to verify and illustrate such calculations, a simulation tool is developed so that an acoustic image can be obtained and a visual evaluation can be performed.

6.1.1 Virtual Scenario

A virtual scenario, which represents the geometry of an ideal measurement scenario, is generated. For this scenario the following assumptions are considered:

- No reflections from the ground nor other noise sources, apart from the wind turbine, are considered. Thus, only direct sound coming from the turbine reaches the beamformer.
- The wind turbine noise is modelled as static monopole sources despite the sources in a wind turbine might be in motion and of a more complex nature.
- The wind-induced noise in the microphones is not accounted for.
- No atmospheric conditions are modelled.

Geometrical specifications from chapter 5 are introduced:

- Array position and pointing direction: the array is positioned 15 m above the ground, 80 m away from the wind turbine and pointing at a height of 75 m.
- Mapping area position and size: the mapping area is positioned over the wind turbine plane covering 100x120 m.

Figure 6.1 shows the generated virtual scenario. The dark grey rectangle represents the wind turbine area of interest (90x110 m), while the outer light grey represents the mapping area. The red dots depict hypothetical wind turbine noise sources, whose positions are explained in section 6.2. The black dots portray the microphones in the array. The blue line shows the on-axis focusing direction.

6.1.2 System Operation

The system requires the definition of:

- The array geometry: with the microphone positions $\mathbf{r}_m$ and weighting coefficients w_m.
- The source scenario: with the source positions $\mathbf{r}_s$ and their pressure amplitudes P_{0s}.

Once the array and sources are defined, the contribution of all sources in the sound pressure arriving at each microphone is calculated trough the expression:

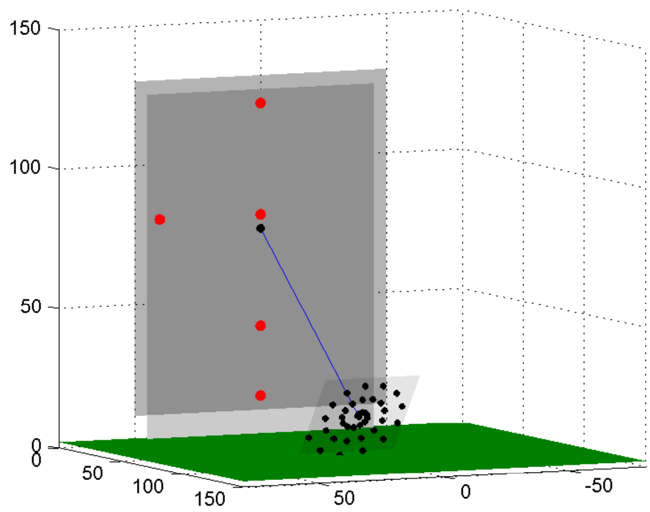

Figure 6.1: Virtual scenario with the wind turbine area of interest (dark grey), the mapping area (light grey) and the microphone array. Sources and microphones are depicted with red and black dots respectively.

$$P_m(w) = \sum_{s=1}^{S} \frac{P_{0s}}{|\mathbf{r}_s - \mathbf{r}_m|} e^{-j\frac{w}{c}|\mathbf{r}_s - \mathbf{r}_m|} \tag{6.1}$$

where P_{0s} is the pressure amplitude of the s'th source, $\mathbf{r}_s$ and $\mathbf{r}_m$ are the position vectors of the sources and the microphones respectively, w is the frequency of study.

Then, the system scans each possible point $\mathbf{r}$ within the mapping plane by the choice of the delays:

$$\Delta_m(\mathbf{r}) = \frac{|\mathbf{r}| - \mathbf{r}_m(\mathbf{r})}{c} \tag{6.2}$$

The pressure at each microphone and the calculated delays are introduced in the beamforming delay-and-sum expression,

$$B(\mathbf{r}, w) = \sum_{m=1}^{M} w_m P_m(w) e^{-jw\Delta_m(\mathbf{r})} \tag{6.3}$$

obtaining one output value for each frequency w and focusing point $\mathbf{r}$. These values are subsequently stored in a two dimensional matrix which is finally plotted as an image. In that image each level of the beamforming output correspond to a different colour where the most powerful sources can be identified. This image is called a *contour plot*.

6.1.3 The Contour Plot

The contour plot is a two dimensional representation, where the relative levels of a certain source distribution are mapped using a colour code. The axes represent the x and y dimensions of the mapped area.

Before the image is generated, the output values $B(\mathbf{r}, w)$ are normalized and converted to dB. The dynamic range of the image is set from 0 to -10 dB, where maximum values (0 dB) are red and minimum values (-10 dB) are blue. Figure 6.2 shows an example of a contour plot. In this figure, the small circles represent the actual location of the sources. As the positions of the noise sources are know beforehand, these circles are plotted as a reference during the design process to give an idea of the accuracy of their identification. The inner rectangle delimits the wind turbine area of interest.

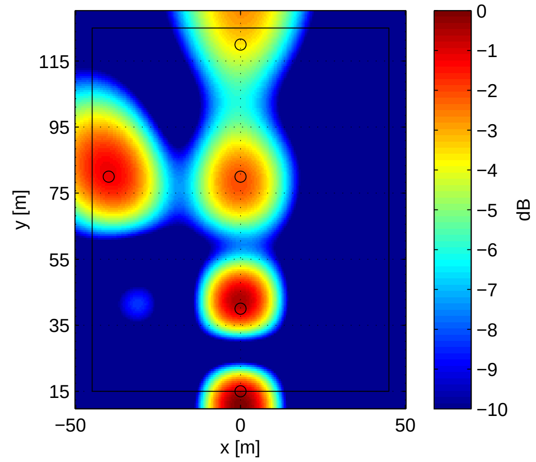

Figure 6.2: Example of a contour plot.

From the contour plot, the behaviour of any array geometry can be tested. Any source distribution can be defined to evaluate the resolution and the dynamic range in a visual way.

6.1.4 Spherical Divergence

The simulation gives the possibility to decide if the spherical divergence of the sound is simulated or not, only by removing the term $\frac{1}{|\mathbf{r}_s - \mathbf{r}_m|}$ from equation 6.1. It can be of interest to study the radiation of the sources at their origin instead of at the measurement point. Figure 6.3 shows the influence of simulating the spherical divergence in a contour plot. Note that the sources in the higher part of the acoustic image are more attenuated since their distance to the array is longer.

It has been decided not to take the spherical divergence into account for the simulations, since the relative level differences among different sources are to be analysed, and their contribution at their origin is more suitable for this matter.

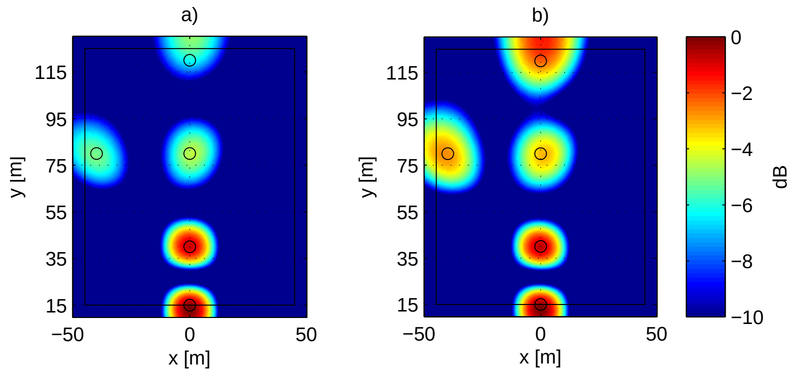

Figure 6.3: Contour plots using a grid array of 400 microphones and $D = 40$ m at 40 Hz. a) The spherical divergence is taken into account. b) The spherical divergence is not taken into account.

6.2 Design Criteria

The design criteria are based on the requirements for frequency range, resolution and dynamic range presented in section 5.3. Those requirements are to be verified in a simulation obtaining a contour plot where different source distributions can be tested. Besides, estimations of these simulation results can be obtained by calculation of the resolution and the maximum side lobe level function described in chapter 4.

6.2.1 Resolution

According to the requirements set in section 5.3, the resolution must be enough so that the system can resolve, at least, two monopole sources placed 40 m away from each other.

In order to verify this requirement five hypothetical sources are defined as depicted in figure 6.4. The opening angles and measurement distances from the array centre to these sources are included in table 6.1. This source distribution is denoted as *resolution source scenario*. Sources 1 and 2 represent possible noise sources produced by the outer part of the blades. Source 3 is placed in the rotor hub position. Source 4 represents the interaction between the blades and the tower and source 5 a possible source caused by the radiation of the tower. If a beamformer is able to separate such sources, it is considered to be able to discriminate the noise radiation coming from the hub, the blades or the tower of the wind turbine.

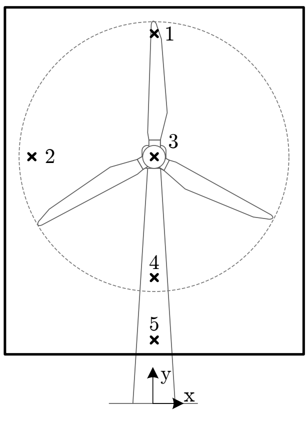

Figure 6.4: Resolution source scenario. Sources 1 and 2 represent possible noise sources produced by the outer part of the blades in the worst case of distance and opening angle. Source 3 is placed in the rotor hub position. Source 4 represents a source caused by the interaction between blade and the tower whose radiation is represented by source 5.

Source number	1	2	3	4	5
Measurement distance z [m]	132.0	110.5	103.0	83.8	80.0
Vertical opening angle θ_V[°]	15.8	2.1	2.2	-19.5	-36.8
Horizontal opening angle θ_H[°]	0	21.2	0	0	0

Table 6.1: Opening angles and measurement distances from the array centre to the sources in the resolution scenario.

Resolution Criterion in a Contour Plot

Two adjacent sources are considered to be resolved when the level difference between the peak of the weakest source and the minimum towards its adjacent is, at least, 2 dB. This value has been obtained empirically by inspection of two adjacent sources in a contour plot. It is considered a sufficient level difference to visually accept that the sources are separable, as long as the image dynamic range is set from 0 dB to -10 dB. Figure 6.5 shows three contour plots where two monopole sources separated are 40 m. The sources are considered just separable when a 2 dB minimum is found between them.

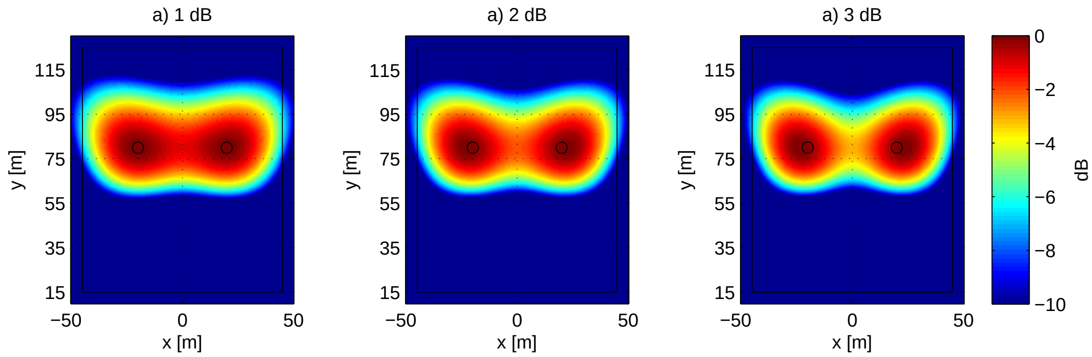

Figure 6.5: Contour plots of two sources separated 40 m with a grid array of 200 microphones at 40 Hz. a) D= 30.4 m, 1 dB between the sources. a) D= 31.5 m, 2 dB between the sources, sources are considered just separable. a) D= 32.4 m, 3 dB between the sources.

Resolution Criterion Through the Estimation of R_k

Another method to validate the resolution of a beamformer is by means of the estimation of the resolution in terms of wavenumber R_k.

It has been observed that the estimation of R_k through the FWMH applied to the squared value of the array pattern (see resolution in section 4.5) is the most consistent method when compared with the results obtained in a contour plot by simulations. That is, obtaining similar contour plots in terms of visual resolution for different arrays lead similar values of R_k measured through mentioned method, while for other calculation methods, R_k values show variation.

When more than 2 dB are measured through the previous criterion, the estimated value for R_k lies bellow 0.2 rad/m. This relationship has been tested for different source scenarios and several array geometries.

Hence, the measure of the main lobe R_k could be used for verification of the requirement fulfilment. In practise, however, this measure does not bring much advantage since the information provided is considered less reliable than the visual inspection and measures over the contour plots.

6.2.2 Dynamic Range

According to the beamforming theory (chapter 4), the dynamic range of an array is derived from the maximum side lobe level (MSL) at the highest frequency. The MSL at 200 Hz is required to be at least -10 dB (cf. section 5.3).

Two ways to verify this requirement are described in the following.

Dynamic Range Criterion in a Contour Plot

In order to verify that the dynamic range requirement is met by inspection of the contour plot of a simulation, the most unfavourable scenario is defined. That is, when a source is placed at the most distant point from the on-axis focusing point in the source map, since it is known form the theory that the side lobe level increases when increasing the focusing angle. Therefore four sources are placed alternatively as depicted in figure 6.6 so that the worst situations are considered. Sources 1 and 2 contemplate the worst cases for the MLS in x and y direction while sources 3 and 4 are only considered in cases where the array pattern is asymmetric. The opening angles and measurement distances from the array centre to these sources are included in table 6.2. Then, from inspection of the contour plot at 200 Hz, the MSL is obtained from the level difference between the peak caused by the source and the second highest level in the contour plot. This difference must be at least 10 dB to meet the requirement [†].

Dynamic Range Criterion Through the Calculation of the MSL

Another method to check the dynamic range requirement is using the MSL function presented in beamforming chapter 4. From this function the maximum side lobe level is evaluated in the worst case, i.e. the maximum opening angle at maximum frequency,

[†]As explained in the specifications (section 5.3), the MSL is not equivalent to the dynamic range of the system, but is considered an indicator of it.

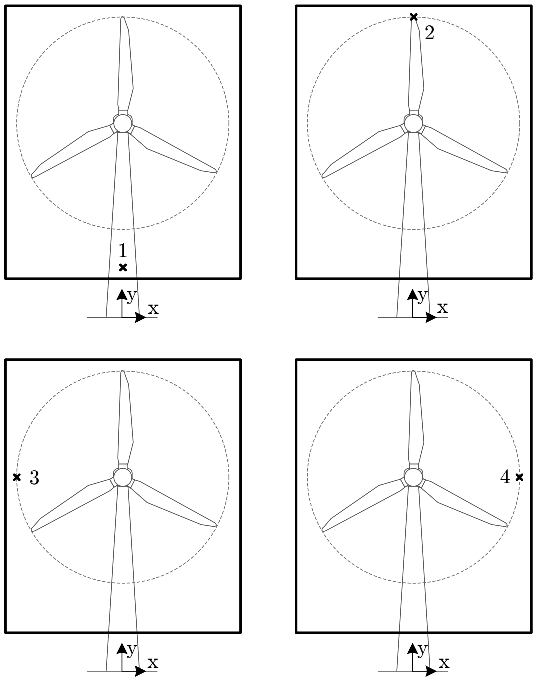

Figure 6.6: MSL sources scenario. Sources 1 and 2 contemplate the worst cases for the MLS in x and y direction while sources 3 and 4 are only considered in cases where the array pattern is asymmetric.

Source number	1	2	3	4
Measurement distance z [m]	80	136.0	109.0	109.0
Vertical opening angle θ_V[°]	-36.8	17.1	0	0
Horizontal opening angle θ_H[°]	0	0	-23.6	23.6

Table 6.2: Opening angles and measurement distances from the array centre to the sources in the MSL source scenario.

where $K^{\theta}_{max}(w_{max})$ is defined. The MSL function can be calculated for both directions x and y and its value must be less than -10 dB in both cases.

This way to check the MSL can serve as a guideline prior to perform any simulation, but it must never be conclusive since the side lobe structure is only studied in x and y directions, while other directions are not considered. Certain array patterns cannot be characterized by their study in x and y, as the most prominent and problematic side lobes are encountered for other directions. Figure 6.7 shows the three dimensional array pattern of a cross array with 100 microphones and size 40 m. Figure 6.8 depicts the radial profile and MSL functions in x and y direction of the same array. Note how those MSL functions in x and y do not contemplate the side lobe structure of the X-cross array, where the higher side lobes are encountered in the directions of the microphone positions. Thus, if an array geometry is validated only by inspecting the MSL function in x and y directions, ghost images are prone to appear in the acoustic image as depicted in figure

6.9.

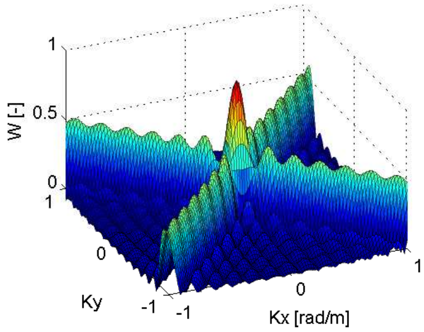

Figure 6.7: Three dimensional array pattern of a X-cross array with 100 microphones and aperture size of 40 m.

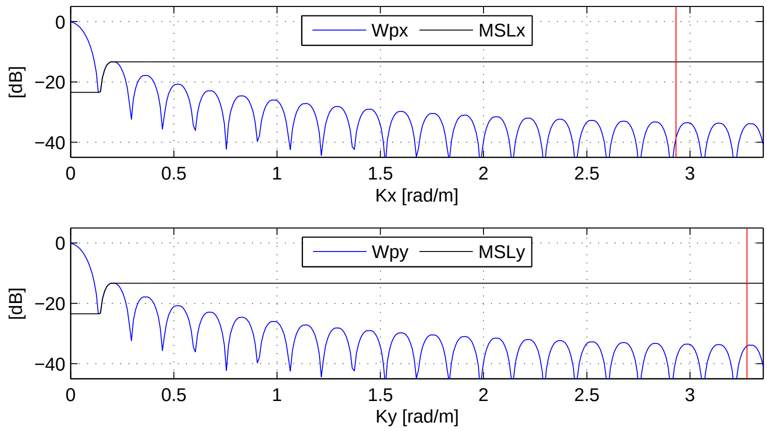

Figure 6.8: Radial profile and MSL functions in x and y direction of a X-cross array with 100 microphones and aperture size of 40 m. The red line represents $K^{\theta}_{max}(w_{max})$, limit of the active part of the array pattern (equation 4.20 in section 4.4.1).

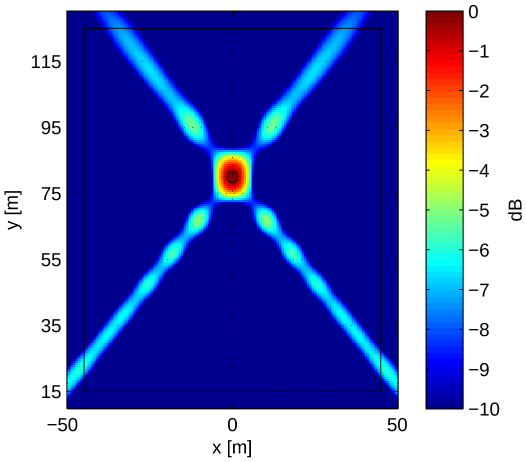

Figure 6.9: Contour plot at 100 Hz using X-cross array with 100 microphones and aperture size of 40 m and source positioned in the rotor hub. The presence of ghost images is clearly seen.

Therefore, it can be concluded that the array dynamic range must be checked from the contour plot of a simulation where all directions of the side lobe structure are presented.

6.3 Design Method

The analysis of the different array geometries and the influence of their parameters in the results is tackled through the search of their optimum configuration. This process is based on the theoretical calculations described in chapter 4 and the inspection of contour plots from simulations of different source scenarios.

The array geometries to be analysed are:

- Grid array
- X-cross array
- Radial array
- Spiral array

These geometries are explained in chapter 7. There are two parameters common that influence the results:

- Number of microphones M.
- Aperture size D.

An initial estimation of D and M constitutes the first step of the array design.

1. Theoretical Estimation of D and M

It is convenient to set initial values of both D and M to use them as a benchmark in the adjustment process.

The aperture size D can be estimated through the equation 6.4 for continuous apertures, where D is directly proportional to the measurement distance z, while inversely depends on the opening angle θ and the frequency f. In order to obtain the most restrictive value, the unfavourable scenario must be considered. Source number 5 in figure 6.4 at 40 Hz, represents this case. Although it is the closest source to the array, its opening angle is the largest among all (see table 6.1), making the term $z/\cos^3(\theta)$ become maximum.

$$D = \frac{a}{R}\frac{z}{\cos^3(\theta)}\frac{c}{f} \tag{6.4}$$

$$D = \frac{1.22}{40}\frac{80}{\cos^3(36°)}\frac{343}{40} \approx 40 \tag{6.5}$$

The initial estimation of M is set for each geometry, since the microphone density depends on the geometrical definition of each array.

After that, the resolution in terms of wavenumber R_k and the MSL function are calculated. These calculations are made according to the expressions described in chapter 4. M is adjusted until the MSL at 200 Hz is below -10 dB while D can be verified so that it gives $R_k < 0.2$.

2. Adjustment of D and M through Simulations

As it is mentioned in section 6.2, the theoretical calculations might not precisely represent the actual performance of the beamformer. This performance is verified by means of simulations in different source scenarios, and the resulting contour plots are analysed. In that way, resolution and dynamic range can be measured visually according to the criteria defined in section 6.2.

3. Optimization of M

The microphones in the previously listed arrays, are placed according to the parametric definitions of the different geometries. For instance, the microphone positions in a spiral follow the curve described by the spiral formula, or the microphones in the radial array are positioned equidistantly in different lines with a common centre.

These locations do not ensure that all microphones are relevant to the overall behaviour of the beamformer, i.e some microphones might give redundant information. Hence, in this step an optimization of M is realized removing the unnecessary microphones preserving the performance of the beamformer. How this optimization is carried out depends on each geometry and is further explained in the following chapter 7.

Chapter 7

Array Geometries

In this chapter, the influence of the geometrical disposition of the microphones within the array for a delay-and-sum beamformer is studied. Different geometries are described and tested so that their optimum configuration can be achieved.

Once the optimum parameters are set for each array geometry, a comparison among them is performed and the most suitable one is selected. The analysis and results for each geometries are shown, finishing with a discussion not only considering their performance, but also the cost-effectiveness and practical limitations of the suggested solutions.

7.1 Grid Array

The array consists of a grid of microphones separated a certain distance in both axis. The separation between microphones is denoted as d_x or d_y, x and y axis respectively. The total dimension of the grid is D_xxDy. These distances are depicted in figure 7.1, which represents the microphone positions in a $D_x = 20$ m, $D_y = 15$ m, $M_x = 5$ and $M_y = 7$ grid array.

The separation d between microphones in a line can be calculated as

$$d = D/(M_{line} - 1) \tag{7.1}$$

being M_{line} the number of microphones in this line. The total number of microphones is the multiplication of the number of microphones in both axes, i.e. M_xxM_y.

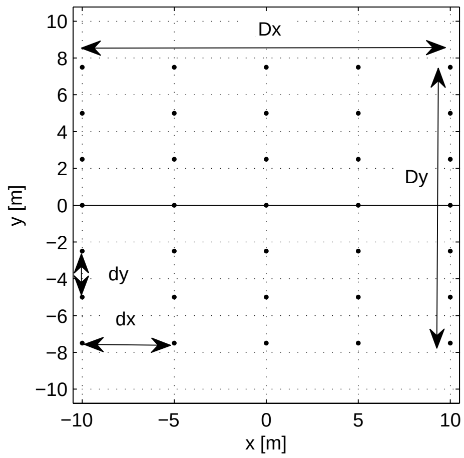

Figure 7.1: Example of the microphone positions in a $D_x = 20$ m, $D_y = 15$ m, $M_x = 5$ and $M_y = 7$ grid array.

1. Theoretical Estimation and Adjustment of D and M

Array Size D The microphones in the array can form a square or a rectangle. A rectangular configuration, meaning $D_x \neq Dy$, is recommended when different resolutions are desired in x- and y-axis. For instance, if more resolution in the y-axis is needed, D_y should be larger than D_x. Nonetheless, this is not the case in the actual wind turbine scenario, where the same spatial resolution in both axis is required. Thus, a square array of size D is selected for the analysis.

An initial approximation of D is estimated according to expression 6.5, leading to $D = 40$ m.

Distance between microphones d From beamforming theory, it is known that the spacing between microphones in regular arrays determines the appearance of grating lobes within the visible area (cf. section 4.1.2). Knowing D and the number of microphones M, the distance between them d can be calculated. In order to avoid the appearance of grating lobes, the distance between two microphones should be

$$d_{max} = \pi / k_{max} \tag{7.2}$$

where k_{max} is maximum wavenumber and can be calculated as,

$$k_{max} = \frac{\omega}{c} \sin(\theta_{max}) \tag{7.3}$$

The estimation of d is done for the maximum frequency and the most unfavourable scenario regarding θ, resulting in

$$k_{max} = \frac{2\pi\ 200}{343} \sin(36°) = 2.19\ [rad/m]$$

Inserting this value in equation 7.2, the maximum distance to prevent for aliasing at 200 Hz is 1.4 m.

Number of Microphones M Once D and d are calculated, the value of M_{line} can be worked out from equation 7.1.

$$M_{line} = \frac{40}{1.4} + 1 \approx 29 \text{ microphones}$$

Thus the theoretical number of microphones in the array is $M = 29^2 = 841$.

MSL and resolution in terms of wavenumber R_k using a grid array of $D = 40$ m and $M = 841$ are calculated, leading to $R_k = 0.1340$ rad/m and $MSL = -13.24$ dB. The MSL requirement is fulfilled, and R_k is below the suggested threshold of 0.2 rad/m, suggesting that M and D are overestimated.

M is reduced until aliasing appears in the active part of the array pattern. Accordingly, D is reduced so that equation 7.1 still holds, resulting in a $D = 35$ m and $M = 21^2 = 441$. The radial profile and the MSL function of such beamformer are depicted in figure 7.2. The MSL function is below -10 dB, fulfilling this way the MSL requirement.

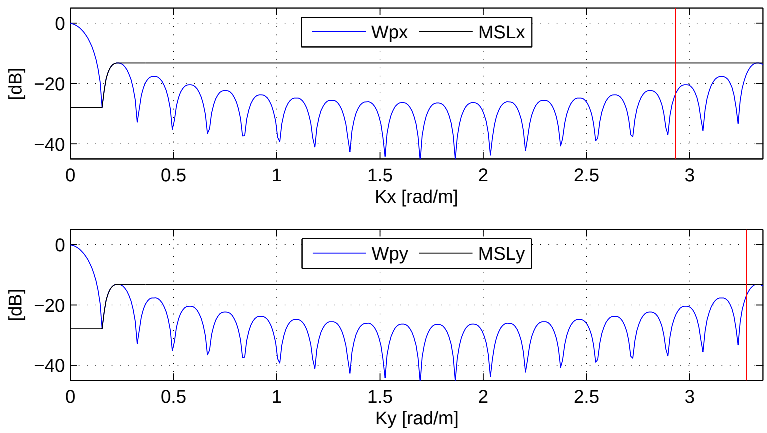

Figure 7.2: Radial profile and the MSL function of a grid array of $D = 35$ m and $M = 21^2 = 441$. The red line represents $K^{\theta}_{max}(w_{max})$, limit of the active part of the array pattern (cf. section 4.4.1).

2. Adjustment of D and M through Simulations

The array reached up to this point has $D = 35$ m and $M = 441$. It is simulated in the resolution and MSL source scenarios. The resolution meets the requirement, since it is possible to clearly resolve sources placed 40 m from each other, even at 40 Hz. Simulations are also performed decreasing the values of D, leading to a substantial worsen of the resolution. Thus, D is fixed to 35 m.

The MSL requirement is also met with $M = 441$. Arrays with $D = 35$ m, but less number of microphones are simulated. From these simulations, it can be seen how aliasing start to appear when M is decreased to 361 (19^2) microphones. This situation is depicted in figure 7.3a, where a ghost image appears in the y-axis. Hence, M is set to 400 (20^2) . Figure 7.3b shows how the MSL requirement is met for such array.

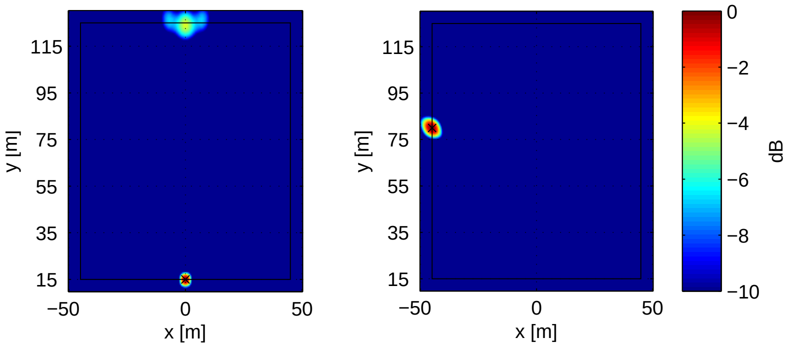

(a) M = 361 microphones.

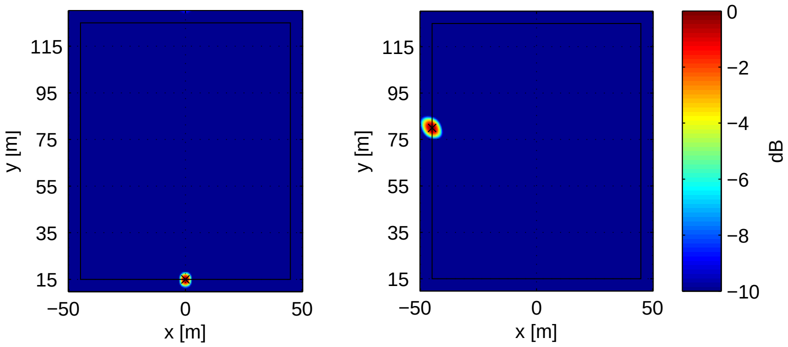

(b) M = 400 microphones.

Figure 7.3: Acoustic images obtained at 200 Hz using the selected grid array of $D = 35$ m and $M = 361$ and $M = 400$ respectively. Sources 1 and 3 of the MSL source scenario.

Figure 7.4 shows the acoustic images obtained at 40, 100 and 200 Hz using the selected grid array ($D = 35$ m and $M = 400$ microphones) for the resolution source scenario. It can be seen than all sources can clearly be localized. In the acoustic image at 40 Hz, the interaction of the first side lobe of the array pattern when the beamformer is focusing at sources 2 and 3, can be seen. This unavoidable interaction causes the appearance of a ghost image.

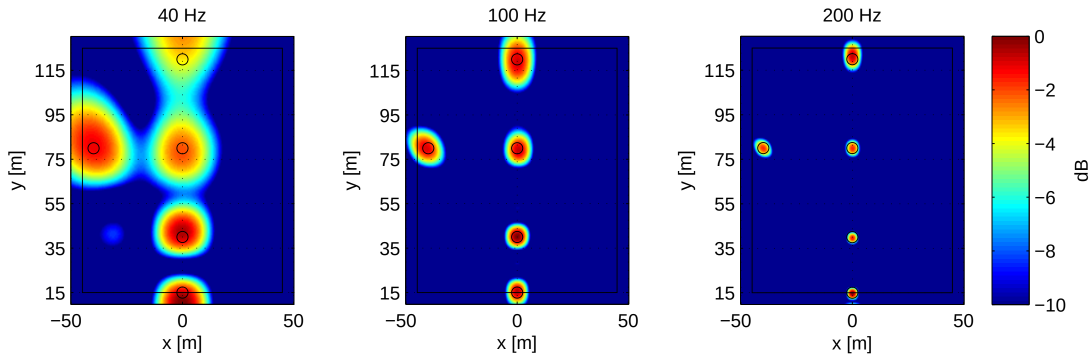

Figure 7.4: Acoustic images obtained at 40, 100 and 200 Hz using the selected grid array of $D = 35$ m and $M = 400$ microphones. Resolution source scenario.

3. Optimization of M

Up to this point, a grid array with the following set-up has been reached:

- Array aperture size: $D = 35$ m.
- Number of microphones: $M = 400$.

Different Microphone Spacing $d_x \neq d_y$

In order to optimized the number of microphones in a grid array it is possible to use different number of microphones in x and y axis. Since the maximum off-axis angles is larger in the y axis than in the x axis (see table 6.2), the maximum spacing between microphones (before aliasing occurs) in the x axis is less restrictive, $d_x > d_y$. This option is investigated leading to an optimum result of $M_x = 19$ and $M_y = 20$, i.e. $M = 380$ microphones.

Figure 7.5 shows the acoustic images obtained at 40, 100 and 200 Hz for the resolution source scenario. As it happened in the previous case (figure 7.4), it can be seen that all sources can clearly be localized. An improvement of 20 microphones is achieved.

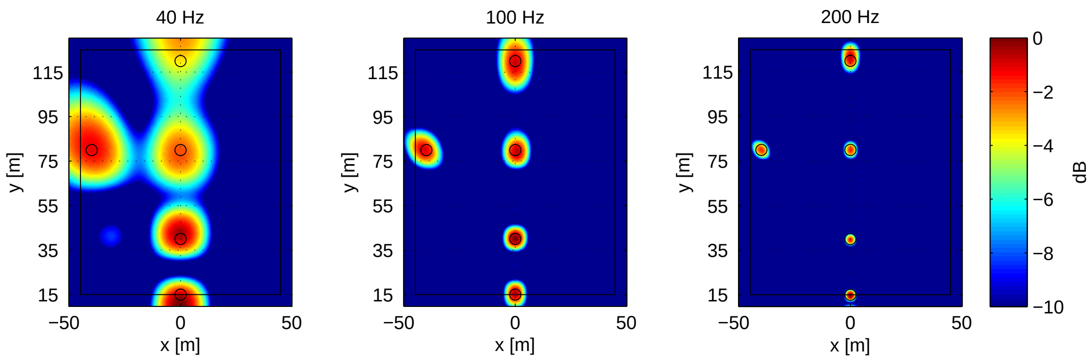

Figure 7.5: Acoustic images obtained at 40, 100 and 200 Hz using the selected grid array of $D = 35$ m, $M_x = 19$ and $M_y = 20$ microphones. Resolution source scenario.

Frequency Bands Optimization

Another approach to optimize the number of microphones is based on the fact that:

- The minimum frequency of interest determines the array size D.
- The minimum spacing between microphones has to the such that no aliasing occurs. This spacing depends on the frequency (equation 7.2); the higher the frequency, the less distance between microphones.

In the grid array previously defined ($D = 35$ m and $M = 400$ microphones), D was fixed to meet the resolution requirement at 40 Hz. The number of microphones, however, were selected so that the dynamic range requirement was met at 200 Hz. This situation suggests the idea of dividing the structure of the microphones and the processing of the beamformer in frequency bands.

As a first approximation of this philosophy, two frequency bands are studied independently. The low frequency band ranges from 40 to 100 Hz, whereas the high frequency band ranges from 100 to 200 Hz. Initially and to easy the design process, different arrays for each band are consider independently.

The *low frequency array* uses D that ensures the resolution fulfilment at 40 Hz and the microphone spacing that prevents from aliasing at 100 Hz. Likewise, the *high frequency array* uses D adjusted to 100 Hz and d adjusted to 200 Hz. D and M for these arrays are obtained by means of the simulations, leading to:

- *Low frequency array*: $D = 35$ m and $M = 12^2 = 144$ microphones (figure 7.6a).
- *High frequency array*: $D = 20$ m and $M = 14^2 = 196$ microphones (figure 7.6b).

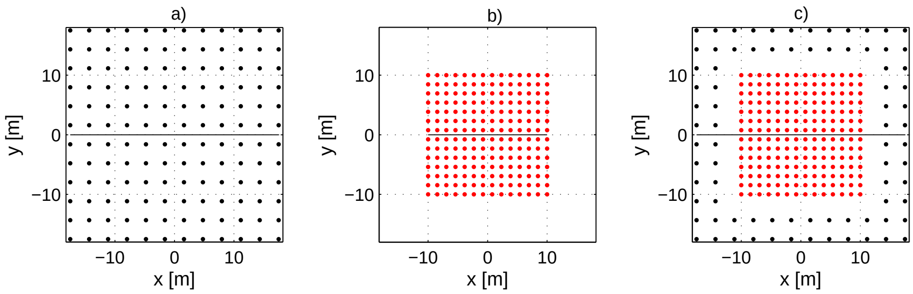

Figure 7.6: Example of a possible implementation for a frequency divided grid array. a) *Low frequency array*: $D = 35$ m and $M = 12^2 = 144$ microphones. b) *High frequency array*: $D = 20$ m and $M = 14^2 = 196$ microphones. c)Resulting grid array $D = 35$ m and $M = 144 + 196 = 340$ microphones. All microphones are used to process the low frequency bands, whereas only the red ones are used to process the higher one.

In figure 7.6, it can be seen that the central area of the low frequency array can be replaced by the whole high frequency array. In that way, the same structure can be used just electronically activating and deactivating the useless microphones depending on the band to process. The resulting microphone positions are depicted in figure 7.6c. The number of microphones is decreased from 400 to 340.

Then all the microphones of the array in figure 7.6c would be used to process the beamformer output in the low frequency band, where as only the microphones in figure 7.6b would be use for the higher band.

The low frequency array is simulated, leading to a poor resolution at 40 Hz. This is caused by the increase of the density of microphones in the centre of the array, which makes the main lobe of the array pattern wider. This density can be decreased by *deactivating* certain microphones in this inner area. This does not imply a decrease in the number of microphones of the total array, since all these microphones need to be in there for the high frequency band. A simulation removing half of the microphones alternatively in the inner area is carried out to verify the improvement. The disposition of the microphones is depicted in figure 7.7. The resulting acoustic images obtained in both bands are depicted in figures 7.8a and 7.8b.

The optimized grid array parameters are summarized next.

- Total array: $D = 35$ m and $M = 340$ microphones (figure 7.6c).
- Low frequency band part: $D = 35$ m and $M = 178$ microphones (figure 7.7).
- High frequency band part: $D = 20$ m and $M = 196$ microphones (figure 7.6b).

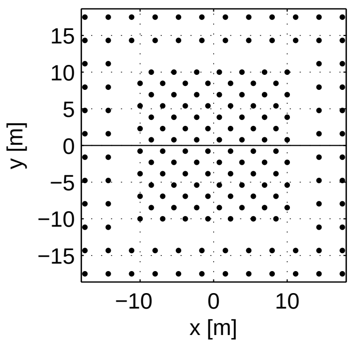

Figure 7.7: Low frequency band part of the optimized grid array, $D = 35$ m and $M = 98$ microphones.

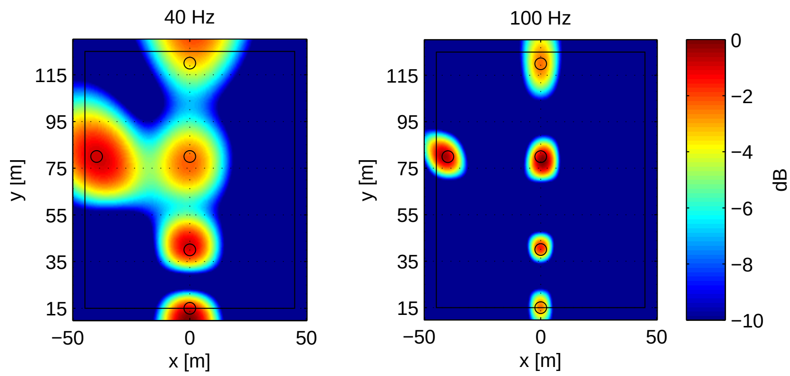

(a) Low frequency band

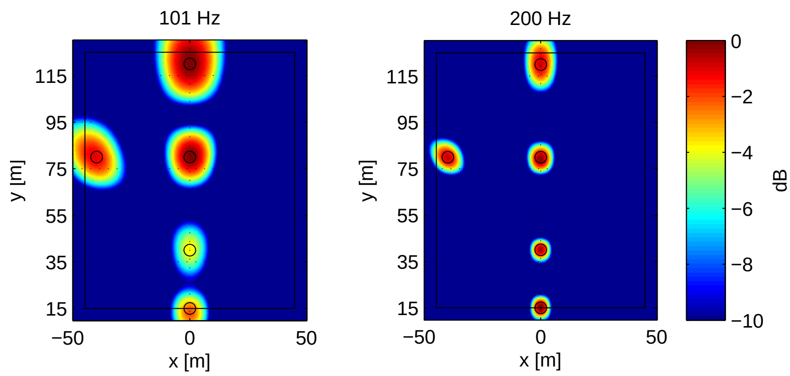

(b) High frequency band

Figure 7.8: Acoustic images obtained for the low and high frequency bands of the optimized grid array of $D = 35$ m, $M = 98$ microphones for the low frequency band and $M = 178$ microphones for the high frequency band. Resolution source scenario.

7.2 X-Cross Array

A X-cross array consist of an arrangement of equidistant microphones disposed in a 45° tilted cross as depicted in figure 7.9.

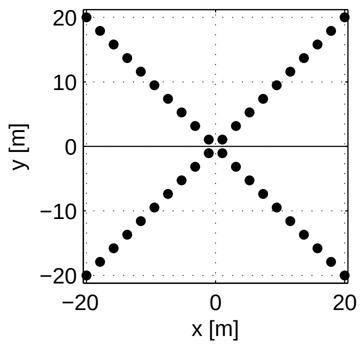

Figure 7.9: Example of the microphone distribution of a cross array of 40 m and 40 microphones.

The design of a X-cross array is motivated from the idea of obtaining a two-dimensional beamformer by the combination of two simple linear arrays.

A linear array can only resolve sources in one direction. Figure 7.10 shows the acoustic image of a simulation using a vertical linear array in the resolution source scenario described in section 6.2.

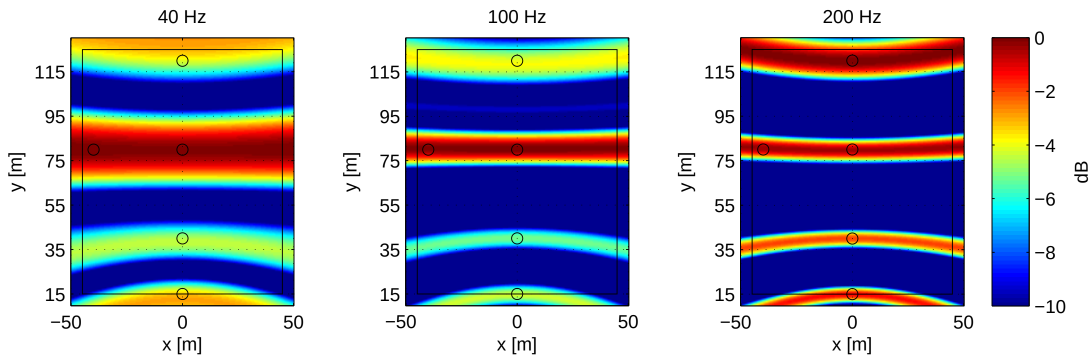

Figure 7.10: Acoustic images obtained with a vertical linear array of 40 m and 40 microphones.

Results are obviously analogous for an horizontal linear array. Through the combination of these two arrays, it is expected that the resulting beamformer will be able to resolve waves in both directions. In fact, the combined array pattern presents a main lobe in its centre, however, unavoidable side lobes remain in the directions of the original linear arrays. Figure 7.11 illustrates such consequence, where the array patterns of two linear arrays are shown, together with the array pattern of their combination.

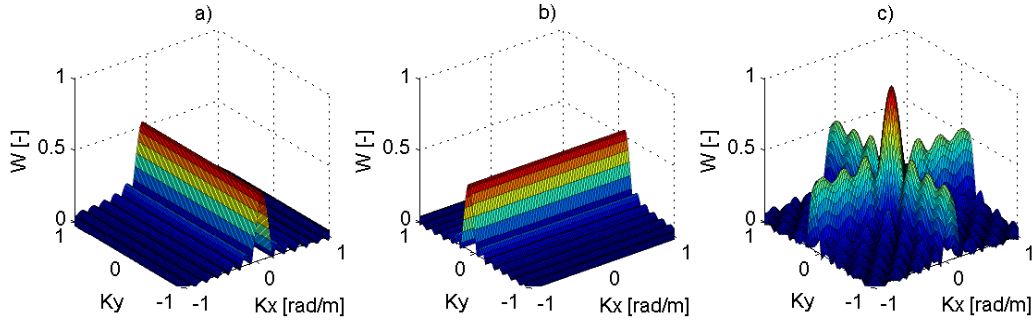

Figure 7.11: a) Array pattern of a linear array disposed along the x axis. b) Array pattern of a linear array disposed along the y axis. c) Array pattern of the combination of previous linear arrays.

Those side lobes are always present with −5 dB respect to the main lobe, no matter the number of microphones used, this value remains constant. Therefore, no more than 5 dB of dynamic range can be obtained for the combination of an horizontal and a vertical linear arrays. When this combined array is tilted 45° to create the aforementioned X-cross array, its side lobe structure remains in the directions defined by the microphone positions. Figure 7.12 shows an acoustic image generated using a X-cross array of 40 microphones with a single source.

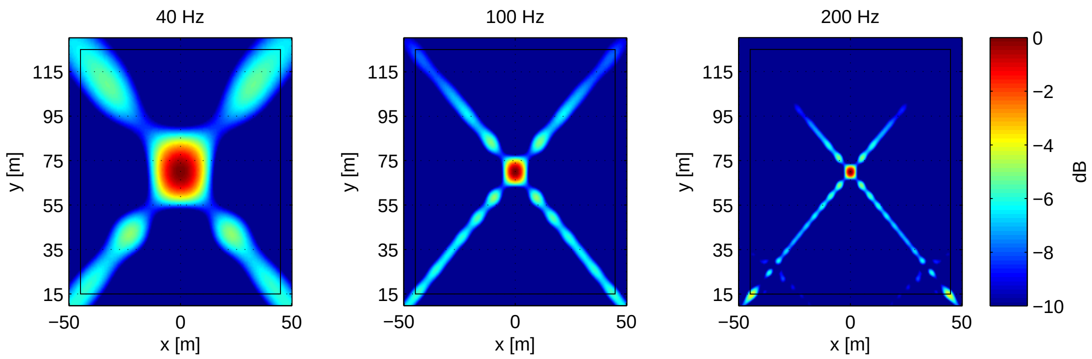

Figure 7.12: Acoustic images obtained with a X-cross array of 40 m and 40 microphones where a single source is placed in the hub.

According to [Brüel&Kjær, 2004], the ghost image problem caused by the side lobes can be to some extent resolved by processing each linear array independently and subsequently combine the results. Nevertheless, this solution is only valid for a single source scenario. If multiple sources are present, the interaction between the side lobes causes unavoidable ghost sources. Figure 7.13 shows the results using a X-cross array in a multiple source scenario.

It is concluded that this array geometry is not suitable for this purpose, where multiple sources are expected to be present in different parts of the wind turbine.

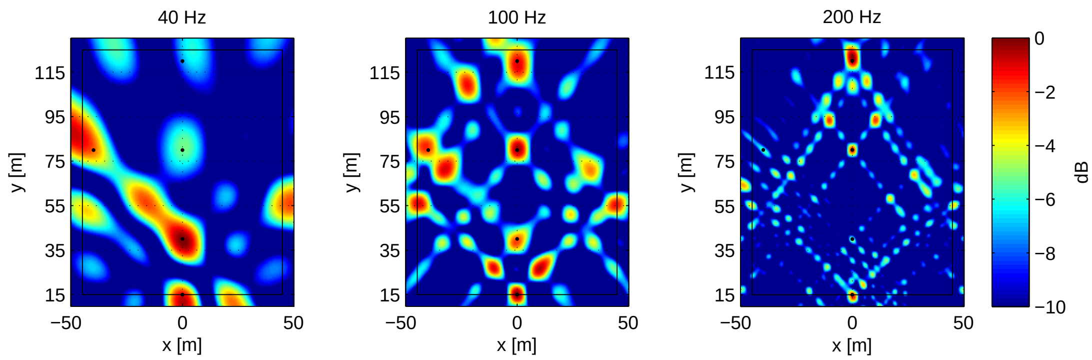

Figure 7.13: Acoustic images obtained with a X-cross array of 40 m and 40 microphones for the resolution source scenario.

7.3 Radial Array

The radial array consist of a combination of linear microphone arrays forming a wheel in which each line constitutes a spoke. The parameters involved in this geometry are:

- Aperture size D.
- Number of microphones M, that can be divided in the number of microphones in each of the spokes Ms.
- Number of spokes N

A typical radial array with 8 spokes is depicted in figure 7.14.

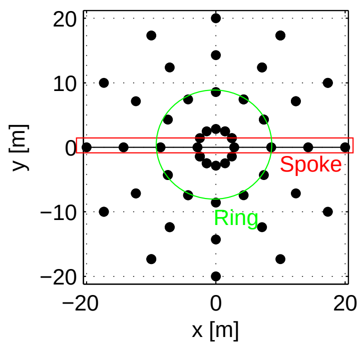

Figure 7.14: Example of the microphone distribution of a radial array of 40 m, 6 spokes and 6 microphones per spoke.

This geometry is motivated from the idea of combining more than two linear arrays to avoid the side lobe problems encountered in the X-cross array geometry (see section 7.2).

In fact, inserting linear arrays in a radial configuration causes a decrease of the side lobes in the directions of the microphone positions. Figures 7.15 and 7.16 show the array pattern of different radial arrays with increasing number of spokes. Each spoke added increases the main lobe level, thus the relative level of the side lobes decreases.

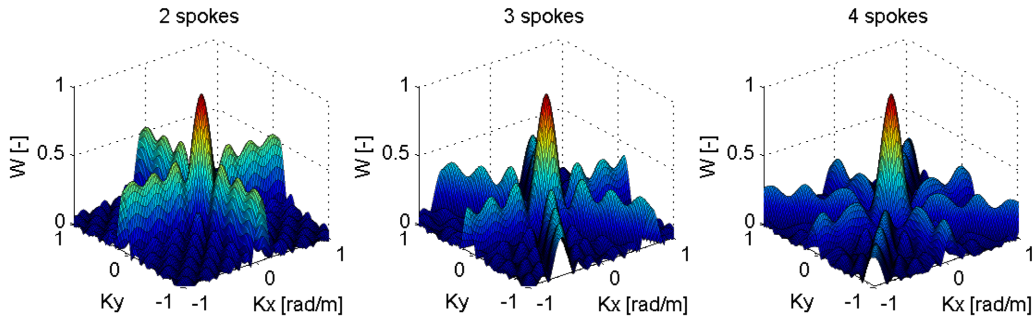

Figure 7.15: Array pattern of a radial array with 2, 3 and 4 spokes.

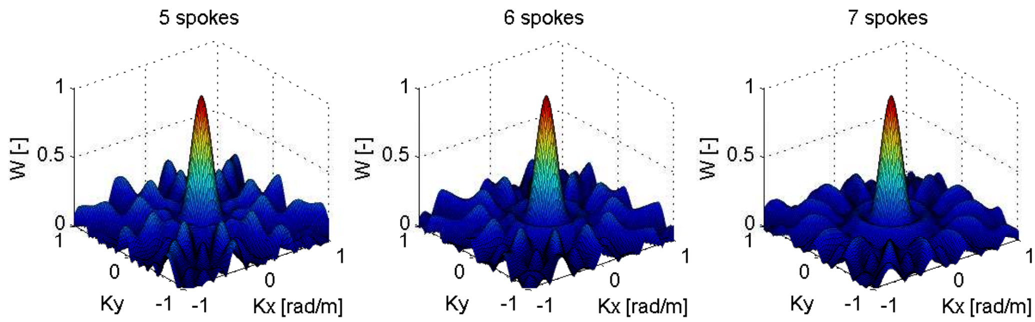

Figure 7.16: Array pattern of a radial array with 5, 6 and 7 spokes.

In this way, an optimal solution can be found by the proper selection of the values for D, Ms and N.

1. Theoretical Estimation of *D*, *Ms*, and Calculation of the Number of Spokes

Aperture Size *D* The aperture size is firstly estimated through the expression 6.4 for continuous circular apertures. As described in section 6.3 An initial value of $D = 40$ m is selected.

Number of Microphones per Spoke *Ms* The maximum distance between microphones d is calculated so that the appearance of grating lobes is prevented. The most restrictive situation is for the spoke located parallel to the vertical axis y. Being this geometry a combination of linear arrays, the minimum distance between the microphones is calculated through the procedure followed for a grid array in section 7.1. Then, the number of microphones per spoke is $Ms = 29$.

Number of Spokes *N* It has been seen from figures 7.15 and 7.16 how the dynamic range of the system improves when increasing the number of spokes, whilst the resolution is considered to remain constant. Calculations of the MSL function are performed with an aperture size of $D = 40$ m and 40 microphones per spoke. A high number of microphones is chosen so that the influence of their density across the spoke is minimized, thus only the influence of the number of spokes takes part. Figure 7.17 shows the MSL values obtained for an increasing number of spokes in the highest frequency and opening angle.

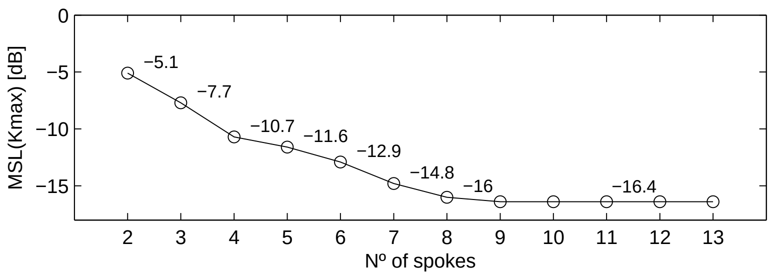

Figure 7.17: MSL of a radial array of $D = 40$ m and Ms =40 microphones with increasing number of spokes.

It can be seen that the MSL does not improve for more than 9 spokes. Then 8 or 9 spokes might be considered enough.

2. Adjustment of *D*, *Ms* and *N* from Simulations

The adjustment of the radial array parameters is not carried out to tightly meet the requirements of the specifications. Instead, they are adjusted with a view on a further optimization process, where the microphones providing with redundant information will be removed. Therefore, some of the contour plots shown in this section have an image dynamic range from 0 to -20 dB so that differences within this range can be perceived when evaluating side lobe presence.

Adjustment of *N* Previous calculations of the MSL for different number of spokes at 200 Hz can be verified through simulations. This is done for source 1 of the MSL source scenario (figure 6.6) defined in the design criteria for dynamic range. Figure 7.18 shows the resulting contour plots at 200 Hz for arrays of the same aperture and microphones per spoke as used for figure 7.17.

Simulations lead similar values than those obtained by the MSL calculation. No improvement is obtained in the side lobes for more than 9 spokes, since a side lobe of constant level -17.2 dB is present. This side lobe is ascribed at the circular disposition of the microphones nearby the centre of the array.

The improvement in the dynamic range using 9 spokes instead of 8 is not considered

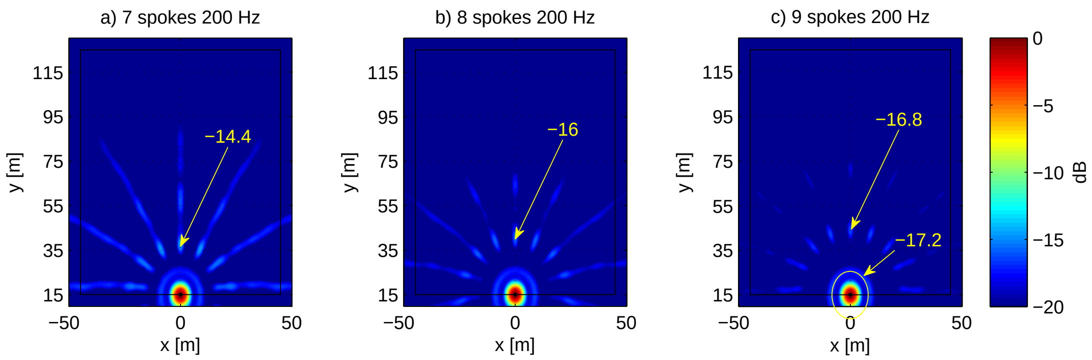

Figure 7.18: Acoustic images at 200 Hz obtained with a radial array of 40 m and 40 microphones per spoke with 7, 8 and 9 spokes respectively. Source 1 of the MSL source scenario. The dynamic range of the image is increased from 0 to -20 dB to illustrate details within this range.

worthy due to the amount of microphones to include. Therefore, the optimum number of spokes is fixed to $N = 8$.

Adjustment of Ms Starting from an initial value of $Ms = 29$ obtained from previous calculations, simulations are carried out for the MSL source scenarios 1 and 3 (figure 6.6) at 200 Hz. The number of microphones per spoke is decreased until ghost images due to the spatial sampling appears within the mapping area. Figures 7.19a and 7.19b show the contour plots of simulations for the limiting number of microphones where aliasing starts to appear.

In light of the results obtained, the number of microphones per spoke is decided to be $Ms = 24$.

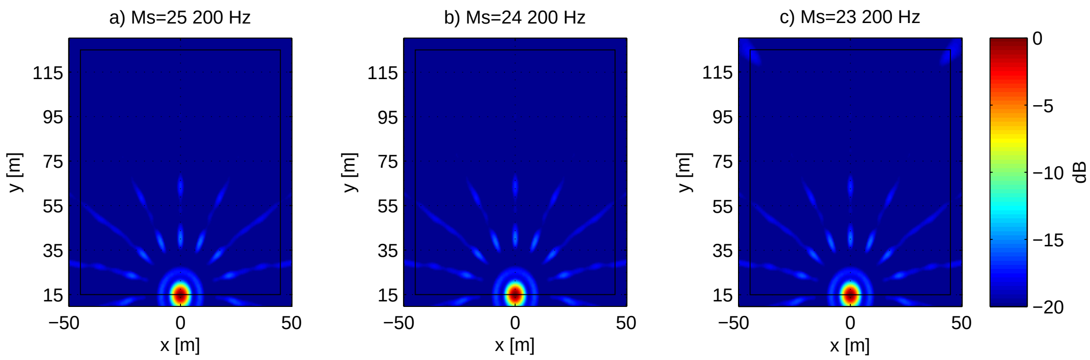

(a) MSL source 1

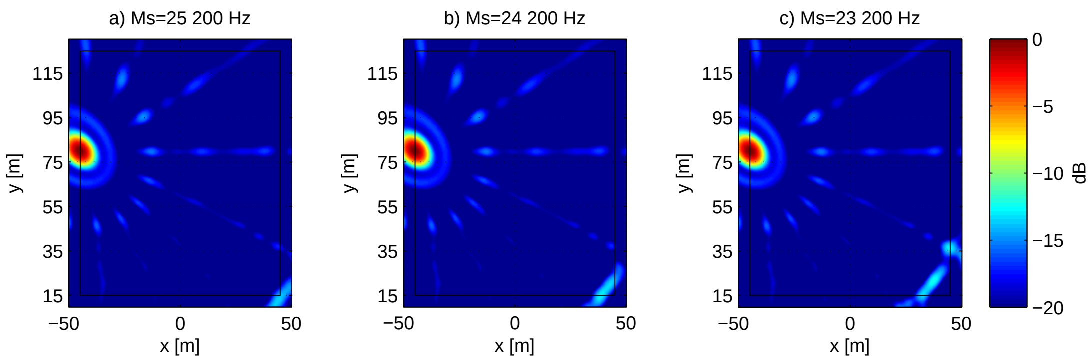

(b) MSL source 2

Figure 7.19: Acoustic images at 200 Hz obtained with a radial array of 40 m and 8 spokes with 25, 24 and 23 microphones per spoke respectively. The dynamic range of the image is increased from 0 to -20 dB to illustrate details within this range.

Adjustment of D The resolution with an aperture size of $D = 40$ m is checked in a simulation at 40 Hz with the resolution source scenario for a radial array of 8 spokes and 24 microphones per spoke. Figure 7.20 shows an acoustic image obtained for such array. The level difference between the weakest source and the minimum between its adjacent source is only 1 dB. However, this initial value of D is considered valid since, as it will be seen in the next section, removing the microphones in the array centre will cause an improvement of the resolution.

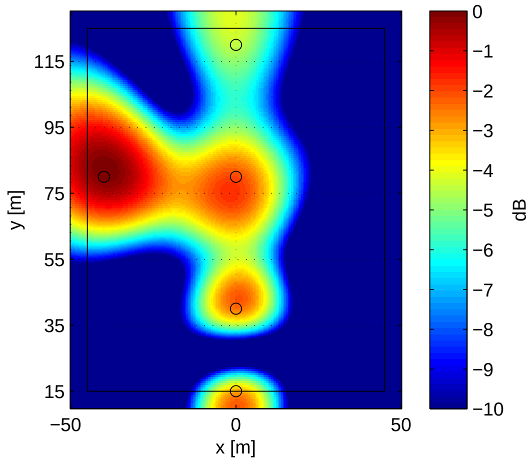

Figure 7.20: Acoustic image generated with a radial array of 40 m, 8 spokes and 24 microphones per spoke at 40 Hz. Resolution source scenario.

2. Array Optimization

Up to this point, a radial array with the following set-up has been reached:

- Array aperture size: $D = 40$ m.
- Spokes: $N = 8$ m.
- Microphones per spoke: $Ms = 24$.
- Total number of microphones: $M = 192$.

This array is depicted in figure 7.21. Its low frequency resolution is slightly lower than the required. The calculated resolution in terms of wavenumber by measuring the main lobe is $R_k = 0.194$ rad/m. It has a dynamic range of around -10 dB in a multiple source scenario despite the MSL is around -16 dB measured for single sources at the MSL source scenario. Figure 7.22 shows simulation results for this array at 40, 100 and 200 Hz.

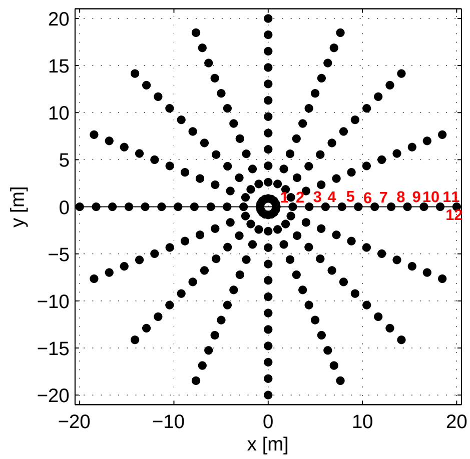

Figure 7.21: Microphone disposition of a radial array of 192 microphones with $D = 40$ m, $N = 8$ m and $Ms = 24$. The microphone rings are numbered from the inner to the outer part to illustrate the optimization process.

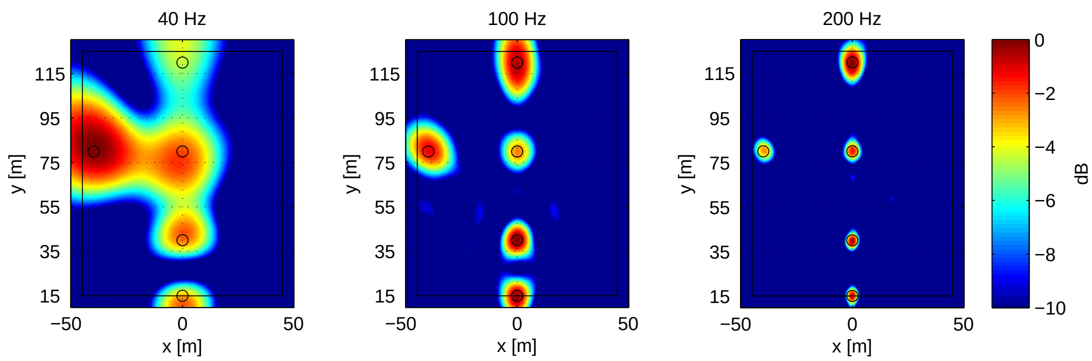

Figure 7.22: Acoustic images obtained with a Radial array of 192 microphones with $D = 40$ m, $N = 8$ m and $Ms = 24$, depicted in figure 7.21.

For the optimization process, the influence of removing the different microphone rings forming the array is analysed. Removing a ring often causes changes in resolution and dynamic range, therefore modifications in both indicators must be evaluated prior to any decision. Rings are removed sequentially in order to tightly meet the requirements stated in the specifications (cf. chapter 5), which are verified according to the design criteria described in section 6.2. The whole optimization process is thoroughly described in appendix A despite a brief description is given in the following.

Removing the Inner Rings Close to the Array Origin It has been observed that the high density of microphones in the inner part of the array causes a widening of the main lobe in the array pattern, thus the resolution can be improved by removing microphone rings number one and two. Then the number of microphones decreases from 192 to 160 obtaining a much better resolution at low frequencies (cf. appendix A).

Removing Rings Systematically Microphones recording redundant information can be removed by studying the influence of each ring alternatively. In this step, the rings number 3, 5, 7 and 9 are removed. Resolution and dynamic range get worse but still meeting the requirements with 96 microphones.

This optimization leads to the array depicted in figure 7.23 with the following set-up:

- Array aperture size: $D = 40$ m.
- Spokes: $N = 8$ m.
- Microphones per spoke: $Ms = 12$.
- Total number of microphones: $M = 96$.

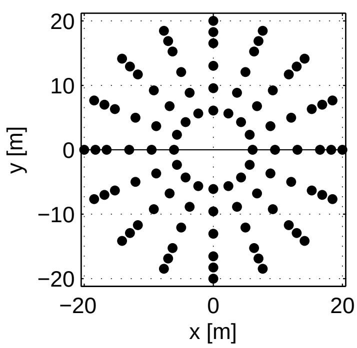

Figure 7.23: Microphone distribution of the optimized radial array of figure 7.21 when the rings 1, 2, 3, 5, 7 and 9 are removed.

Results from simulations with the optimized radial array in the resolution source scenario are shown in figure 7.24.

It must be pointed out that even though the dynamic range at high frequencies is decreased, the MSL requirement is meet obtaining −10 dB in the worst cases. If more dynamic range is required, ring number 9 can be kept, and dynamic range is substantially increased with an array of 112 microphones.

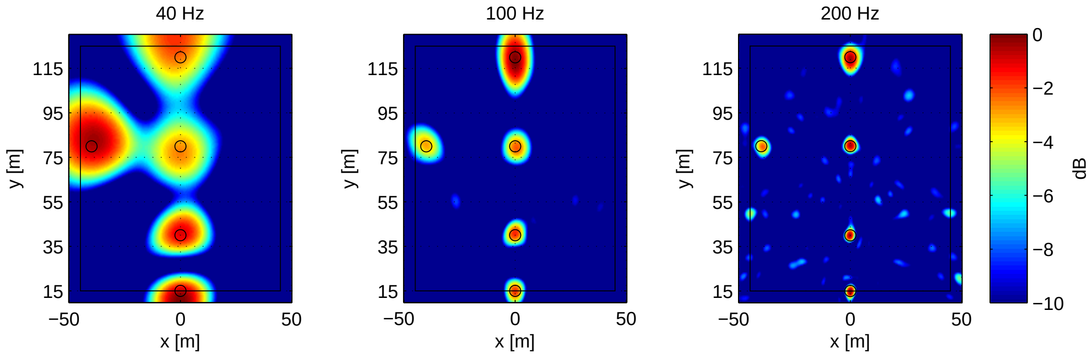

Figure 7.24: Acoustic images obtained with the optimized radial array depicted in figure 7.23 of 96 microphones with $D = 40$ m, $N = 8$ m, $Ms = 12$.

7.4 Spiral Array

The microphones are placed along an Archimedean spiral† for this geometry. A spiral can be seen as a circle which radius increases with the angle. The parametric equation of an Archimedean spiral is:

$$
\begin{aligned}
x &= at\cos(t) \\
y &= at\sin(t)
\end{aligned}
\tag{7.4}
$$

where t ranges from 0 to $n2\pi$, being a n a positive real number, and at is the radius.

According to the way the spiral array is implemented, it does not only have D and M as parameters, but also the number of times the spiral rounds, i.e. the number n that multiplies 2π in the parametric form of equation 7.4. This parameter is refer to as *number of rings* and is denoted as Rn. It determines the separation between the *rings* of the spiral, which is constant and defined as,

$$\text{Rings reparation} = \frac{D/2}{Rn} \tag{7.5}$$

A spiral array of $D = 20$ m, $M = 83$ and $Rn = 5$ is portrayed in figure 7.25 as an example.

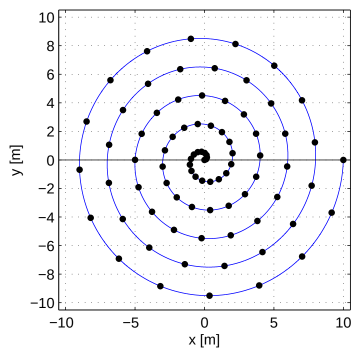

Figure 7.25: Spiral of $D = 20$ m, $M = 83$ and $Rn = 5$.

7.4.1 Number of Rings *Rn*

The number of rings affects the geometrical dispositions of the microphones, modifying their separation. It does not only varies the spacing between rings, but also the spacing

†The Archimedean spiral is sometimes referred to as arithmetic spiral.

between consecutive microphones. This effect can be seen more clearly through the example in figure 7.26, where two arrays with different Rn and $M = 89$ and $D = 20$ m are depicted. Figure 7.26 shows two spirals with five and ten rings. From this example, the following is observed:

- a) Low number of rings. When there are few rings, the distance between adjacent microphones in the centre of the spiral is very short. The spacing between microphones increases as the spiral grows. However, the separation between rings is larger, making non-adjacent microphones be more separated.
- b) High number of rings. As the number of rings increases, the spacing between consecutive microphones enlarges in the central part of the spiral. This distance increases more quickly than in the previous example, resulting in more separated microphones in the outer parts of the spiral. Nonetheless, this separation between rings is smaller, making non-consecutive microphones be closer than before.

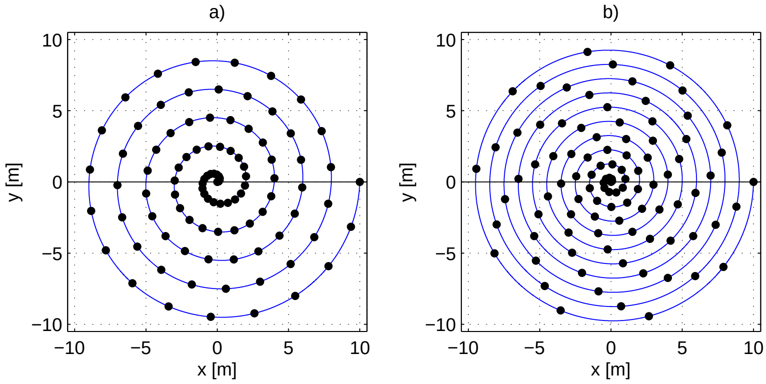

Figure 7.26: Different number of rings in a spiral array of $M = 200$ and $D = 40$. a) Rn is 5. b) Rn is 10.

Besides, certain combinations of M and Rn can cause microphones dispositions with large areas without microphones. This situation is described through the examples in figures 7.27 and 7.28 for a spiral array of $M = 200$ and $D = 40$. It is clearly seen how depending on the the number of rings the microphones are unevenly distributed (figure 7.28), since certain areas not covered by any microphones, while there are directions with too much redundancy. The arrays depicted in figure 7.28 are closer to have a radial disposition rather than a circular one.

This effect occurs depending on the ratio between M and Rn, and a mathematical expression could not be found. Thus, its influence on the results is approached directly by simulations. That makes the search of the optimum parameters a complex task based on

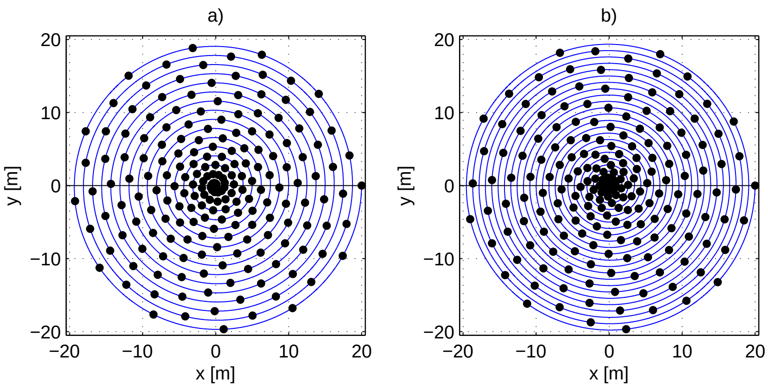

Figure 7.27: Influence on the number of rings in the microphones disposition of an spiral array of $M = 200$ and $D = 40$. a) Rn is 16. b) Rn is 23.

trial and error. In fact, the actual influence of the relation between Rn and M in the resolution and MSL has not been defined. Thus a systematic method cannot be followed for the investigation of this array. Nevertheless, some conclusions can be drawn from the analysis of the resulting acoustic images for different set of parameters.

Influence in the Resolution

When M and Rn are selected in such a way that the resulting microphones distribution is even (like in figure 7.27), the resolution results are independent from Rn. The acoustic images obtained for the these two arrays at 40 Hz can be seen in figures 7.29. This figure shows the same acoustic image for both numbers of rings. However, when the microphones are unevenly distributed, forming a clear radial distribution, the number of rings alters the resolution. In this case, increasing the number of rings means concentrating all the microphones in fewer spokes† as it can be seen in figure 7.28. Simulations for these two arrays are shown in figure 7.30, where it can clearly be seen the worsening of the resolution as the number of rings increases.

†Note that these spokes are not straight lines as in the radial array, but blended ones.

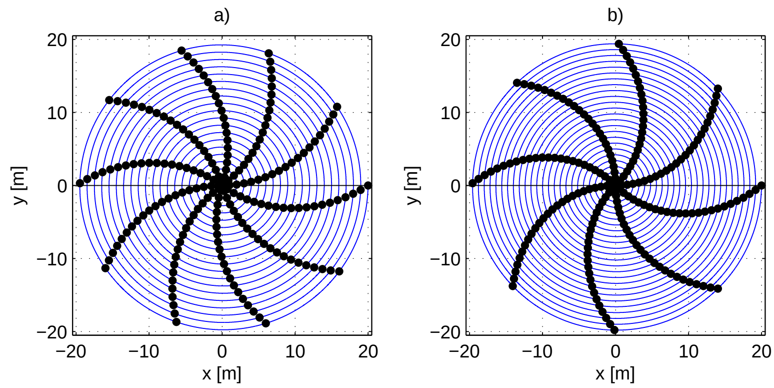

Figure 7.28: Influence on the number of rings in the microphones disposition of an spiral array of $M = 200$ and $D = 40$. a) Rn is 20. b) Rn is 25.

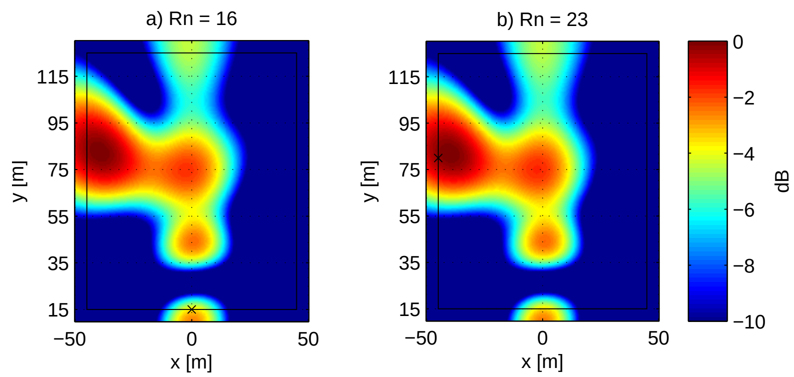

Figure 7.29: Acoustic images obtained at 40 Hz using a spiral array of $D = 40$ m and $M = 200$ microphones. Resolution source scenario. a) $R_n = 16$. a) $R_n = 23$.

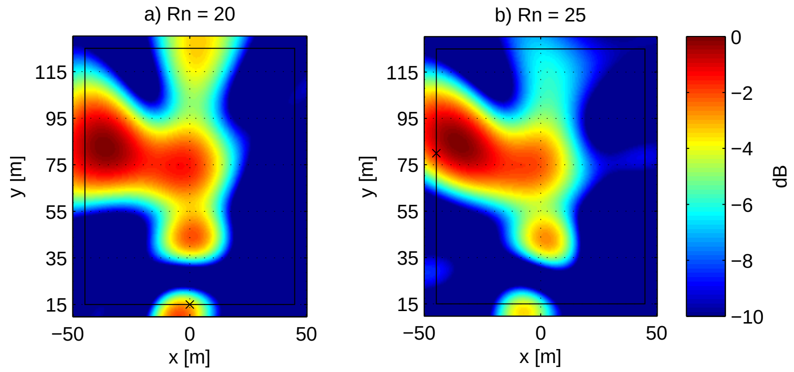

Figure 7.30: Acoustic images obtained at 40 Hz using a spiral array of $D = 40$ m and $M = 200$ microphones. Resolution source scenario. a) $R_n = 20$. a) $R_n = 25$.

In addition, rather high concentrations of microphones in the centre of the array implies a worsen in the resolution in general terms. This can easily be solved decreasing the number of microphone in the areas where the microphones are more densely distributed. This effect is also manifested in the previous examples of regular arrays.

Influence in the Dynamic Range

Several combinations of M and Rn have been tested by means of the simulations and the analysis of the array pattern. It seems that there is not direct relationship between the MSL and the ratio of M and Rn. The array pattern remains mostly unchanged no matter these two parameters†.

7.4.2 Adjustment of D, M and Rn

As it was mentioned earlier, the difficulties encountered in the determination of the optimum number of rings, and its interrelation with M prevent from the use of a systematic analysis method. Therefore, the search of the optimum spiral array lies in a trial and error approach.

D is fixed to 40 m, according to the estimation of expression 6.5. M is set to 250 microphones initially, and number of rings Rn from 5 to 20 are tested. The same process is realised decreasing the number of microphones in steps of 50 microphones until 100. The best results of the simulations are obtained for $Rn = 15$ and $M = 200$ microphones, that are depicted in figure 7.31. The resulting acoustic images for 40, 100 and 200 Hz for the resolution source scenario are shown in figure 7.32. There, it can be seen how the resolution requirement is met at 100 and 200 Hz, whilst it is not at 40 Hz. In that

† M from 100 to 200 in steps of 50 microphones, with Rn from 5 to 25 have been analysed.

frequency, the level difference between the weakest source and the minimum between its adjacent source is only 0.5 dB. However, these results are considered valid, since an optimization is to be performed improving the resolution at low frequencies.

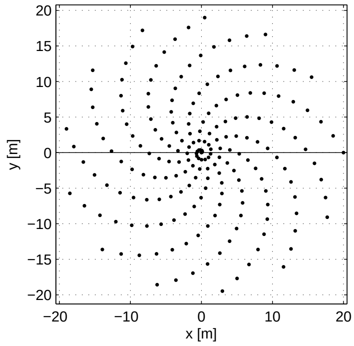

Figure 7.31: Spiral array of $D = 40$ m, $M = 200$ microphones and $Rn = 15$ rings.

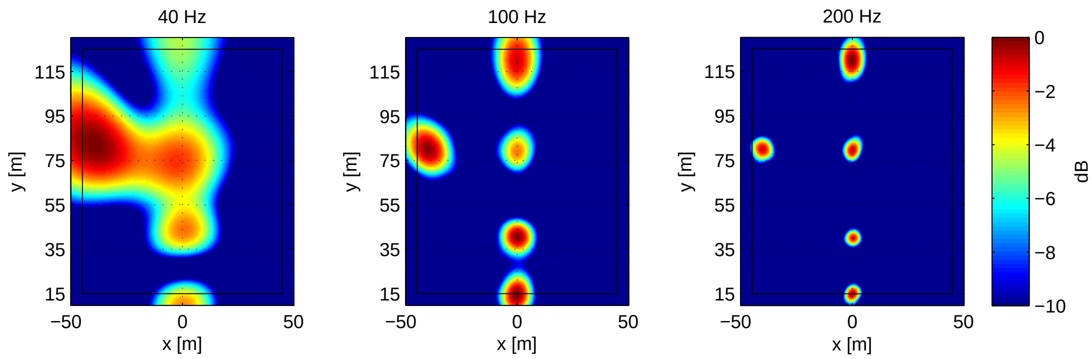

Figure 7.32: Acoustic images obtained at 40, 100 and 200 Hz using the selected spiral array of $D = 40$ m, $M = 200$ microphones and $Rn = 15$ rings). Resolution source scenario.

The fulfilment of the MSL requirement is also verified, confirming that it is met for the four different source position defined for the MSL source scenario.

7.4.3 Optimization of D, M and Rn

The optimization of the spiral array is performed based on the elimination of the possible useless microphones in the array. Besides, it is known that high concentrations of microphones in the centre of the array does not only provide with redundant information, but also worsen the resolution. Thus, as a first approach the microphones of the inner rings are removed meeting a compromised between improvement in the resolution and accurate location of the sources. It has been observed that the first 50 microphones of the spiral can be removed, achieving this way a considerable improvement in the resolution.

Subsequently, more microphones are removed alternatively, however, no rule has been found to determine which microphones should be removed. Simulations are performed to ensure that the requirements are still met.

The array that provides better results after few attempts is found and fixed. It is obtained by removing the first 50 microphones, then from the 51st until the 90th removing one every three, and from the 91st till the 120th removing one every four, resulting in $M = 128$ microphones and $Rn = 15$ distributed as depicted in figure 7.33. The resulting acoustic images at 40, 100 and 200 Hz for the resolution source scenario are shown in figure 7.34. It can be seen how the resolution requirement is met for the three frequencies, achieving this way an improvement in the resolution at low frequencies. Thus, all sources can clearly be identified. The MSL source scenario for the four source positions is simulated as well. These simulations show that the MSL requirement is also met.

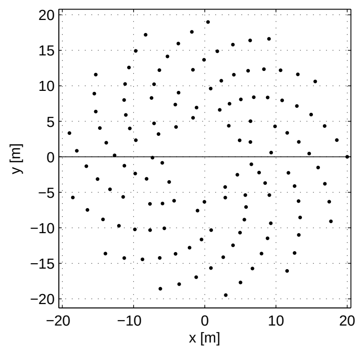

Figure 7.33: Spiral array of $D = 40$ m, $M = 128$ microphones and $Rn = 15$ rings.

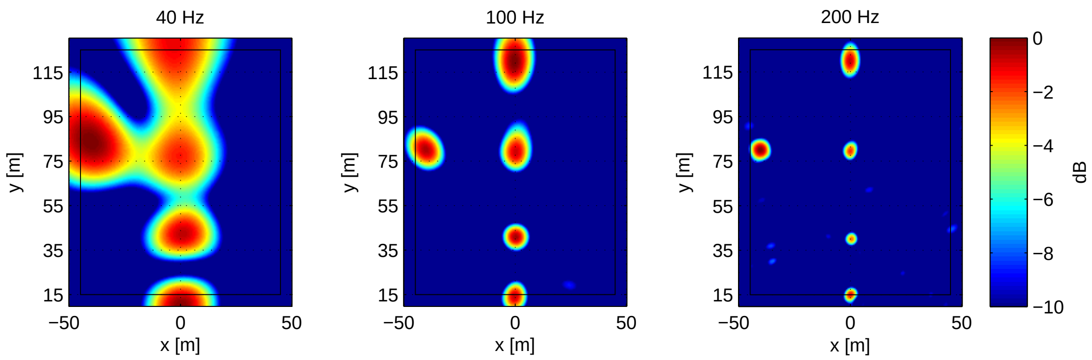

Figure 7.34: Acoustic images obtained at 40, 100 and 200 Hz using the optimised array with $D = 40$ m, $M = 128$ microphones and $Rn = 15$ rings. Resolution source scenario.

7.5 Array Comparison

The following array geometries have been studied:

- Grid Array.
- X-cross Array.
- Radial Array.
- Spiral Array.
- Random Array.

An adjustment and optimization processes have been carried out in order to improve the cost-effectiveness of those geometries. An optimized grid array has been reached with less aperture size and number of microphones, while an optimized radial array has been designed with improved resolution and a great decrease in the number of microphones. The spiral array optimization has also implied a decreased in the number of microphones. This optimization could not be done systematically. Nevertheless, the obtained parameters are considered reasonable to include this array in the comparison.

However, other geometries have been found to be problematic. The X-cross array is not valid for multiple source scenario due to the distribution of its side lobes, causing ghost images in the results (see figure 7.12).

The random array was investigated briefly. It consists of a random distribution of M microphones within a limited area†. Nonetheless, as a systematic approach to its study could not be found due to its inherent random nature, no conclusive results were obtained. Thus the random array is excluded as a possible solution. In addition, random arrays constitute a very inconvenient configuration with a view on a large size outdoors assembly.

Therefore, only the optimum designs reached are suitable for comparisons: optimised grid, radial and spiral arrays. These designs have the following set-ups:

- Optimised grid Array: $D = 35$ m and $M = 340$ microphones.
- Optimised radial Array: $D = 40$ m, $N = 8$ spokes and $M = 12 \times 8 = 96$ microphones.
- Optimised spiral Array: $D = 40$ m, $Rn = 15$ rings and M=128 microphones.

Figure 7.35 shows the resulting geometries and contour plots generated at the limiting frequencies 40 and 200 Hz.

†Typically this area is a circle of radius $D/2$.

Results show the best performance for the radial array concerning the resolution at low frequencies, although both grid and spiral array easily meet the requirements. Source levels at 40 Hz are the most homogeneous for the spiral array, being this feature important when the relative contribution of the sources is of interest. At the higher frequency, it is the grid array which shows the best results, with well localized sources, homogeneous levels and absence of ghost images. The radial array provides the worst dynamic range for that frequency, since its optimization has been based on tightly meet the MSL requirement. It has, however, enough dynamic range to easily identify sources and their contribution.

It must be pointed out that the good performance of the grid array has been obtained for a rectangular aperture of 35 m of side, whereas both radial and spiral arrays cover a circular area of 40 m of diameter, which in practise, will be mounted over a squared structure of 40 m of side. On the other hand, the radial array only requires the use of 96 microphones, a fair number of microphones since it is often a common limitation.

The disposition of the microphones within the array is of great importance when considering large array structures. The microphones in both grid and radial arrays are disposed in a regular basis, where linear structures can be used to attach the microphones leading to a more efficient assembling. In the spiral array, however, microphones are disposed following a complex pattern which leads to an impractical assembling for such large array dimensions.

Gathering all of these considerations, the radial array is considered the best option for the actual scenario, since it provides good resolution at low frequencies and sufficient dynamic range at the highest frequency by only using 96 transducers mounted in a regular structure.

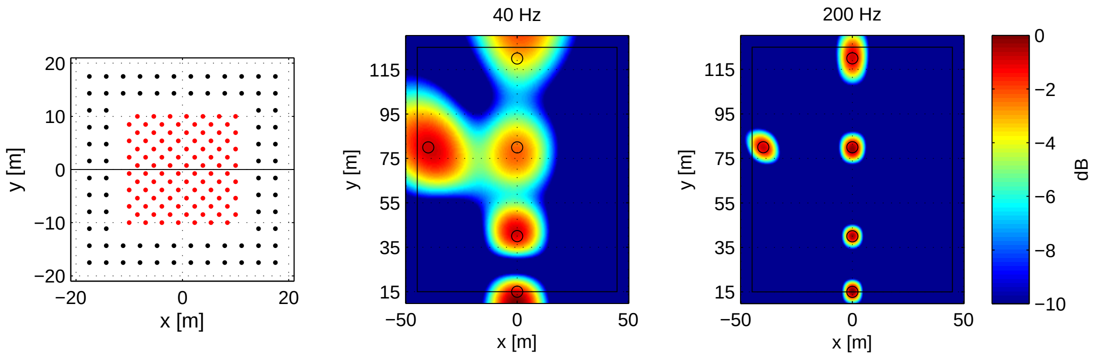

(a) Optimised Grid Array

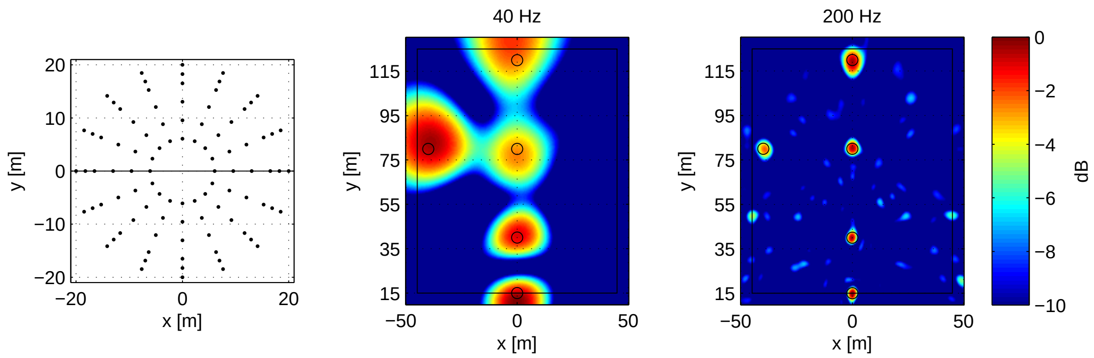

(b) Optimised Radial Array

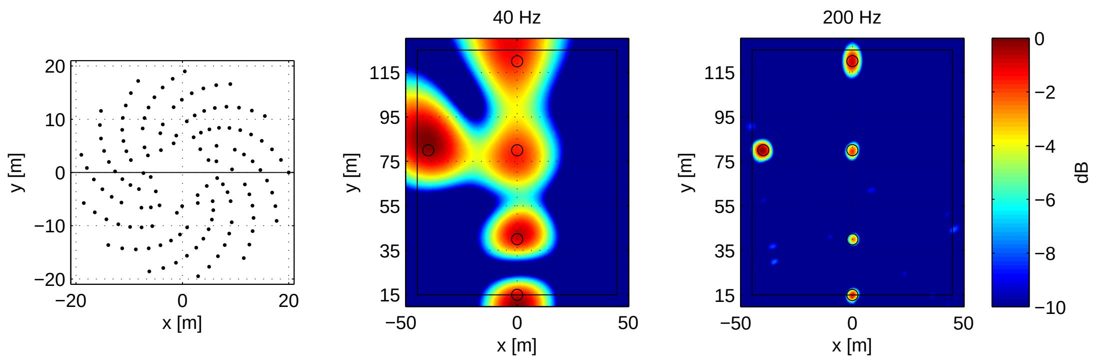

(c) Optimised Spiral Array

Figure 7.35: Microphone positions of the grid, radial and spiral optimised arrays. Acoustic images at 40 and 200 Hz for the resolution source scenario. a) Optimised grid array. b) Optimised radial array. c) Optimised spiral array.

7.6 Summary and Discussion

Throughout this chapter, different array geometries have been studied, tested and adjusted. Optimized versions of each of them have been designed and compared considering their performance and practical aspects.

A regular grid array has been designed starting from theoretical estimations of its aperture size and microphones separation. It has been seen how, due to the different opening angles in each direction x and y, the microphone spacing can be different, adjusting the number of microphones to the real aliasing limitations. Besides, the idea of a multiple frequency band array has been presented, where a two band system has been designed with similar performance and less number of microphones. This frequency-dependent approach could have been used for the other geometries. However, it was only tested for the grid array to check its feasibility.

It has been seen how a linear array can only resolve waves in one direction, whilst a combination of two of them can identify sources in both directions despite its poor dynamic range. This is the case of the X-cross array, which has been considered unsuitable for a multiple source scenario where ghost images make difficult the identification of sources.

The influence of the number of spokes in a radial array has been studied, obtaining that the dynamic range increases up to a certain limit, 9 spokes in this case. Initial parameters of a radial array, aperture size and microphones per spoke, have been set for an optimum performance prior to any optimization. Subsequently, a systematic procedure has been designed for the optimization the array so that it met the stated requirements with the less number of microphones.

The parameters of the spiral array have shown an erratic behaviour that has determined the study of this geometry, since no systematic method could be found to analyse their influence in the results. In spite of this fact, simulations have been carried out for different parameter set-ups, showing fairly good results even when a thorough adjustment has not been possible.

Those arrays have finally been compared in terms of performance and practical aspects. The radial array arises as a good compromise between acoustic image quality and practical implementation. With only 96 microphones it is able to identify multiple sources in a frequency range from 40 to 200 Hz, with a more practical assembling structure.

Chapter 8

Conclusions

The aim of this project was the investigation and determination of the most suitable measurement method to perform acoustic imaging of large structures at low frequencies. A wind turbine was considered an interesting example of a low frequency radiating large structure. Therefore, it was used to hold the investigation of the acoustic imaging measurement method, in terms of geometrical specifications, source distribution and frequency range of interest.

Noise source identification techniques were studied. STSF and beamforming, as two dimensional array based techniques were considered. Despite STSF is traditionally aimed for low frequencies, it requires enormous microphone arrays in order to cover the whole measured structure. Hence, beamforming is found as the optimum choice for large structures acoustic imaging. It allows measurements from medium to high distances, requiring smaller dimensions and less microphones. However, its resolution at low frequencies and long measurement distances was found to be a limitation.

The investigation of the beamforming theory involved the study of certain analysis functions such as the array pattern, the radial profile or the MSL function. It can be concluded that the distance between the microphones determines the upper frequency limit; the dynamic range is derived from the side lobe structure of the array pattern, which is inherent of each array geometry; and the resolution depends on the aperture size of the array.

The error induced assuming plane waves instead of spherical waves must be taken into account for large structures, since the ratio between the array size and measurement distance suggests a near-field situation.

A simulation system was developed to test different array geometries in a particular scenario, where the geometrical specifications of a large wind turbine were modelled. An array design procedure was defined and four geometries were studied.

The best array solution found was the optimized radial array. It provides fair dynamic range and resolution from 40 to 200 Hz only using 96 microphones. However, the dimensions of the array cannot be adjusted to less than 40 m if a minimum resolution is required at 40 Hz. Instead, the grid array geometry can provide good resolution with 35 m of aperture size, however, the amount of microphones required is much larger. It was seen that the X-cross array is not suited for multiple source acoustic imaging, whereas the spiral array was discarded due to the irregular disposition of its microphones.

Therefore, to localize noise sources in a large structure at low frequencies, rather large array sizes are needed. The complexity in the assembly of a slanting measurement structure of this dimensions, or problems derived from the atmospheric conditions, are few examples of the limitations a real application would present, making this solution especially problematic.

Bibliography

Brüel&Kjær. Technical review: Beamforming. 2004.

Brüel&Kjær. Technical review: Non-stationary STSF. 2000.

Brüel&Kjær. Technical review: STSF - a unique technique for scan-based near-field acoustic holography without restrictions on coherence. 1989.

British Wind Energy Association. Noise from wind turbines. The facts. June 2000.

British Wind Energy Association. Low frequency noise and wind turbines. February 2005.

Danish Wind Industry Association. http://www.windpower.org/en/tour/wtrb/size.htm, 2009. Accessed February 2009. Can be found on enclosure CD.

Delta. Low frequency noise from large wind turbines. results from sound power measurements. (AV136/08 Rev. 1), 2008.

B. Ginn et al. A review of array techniques for noise source location. July 2003.

K. Haddad and V. Benoit. Understanding the acoustical behaviour of a wind turbine by means of acoustic imaging. *First International Meeting on Wind Turbine Noise*, October 2005.

IEC 61400-11:2002. Wind turbine generator systems - part 11: Acoustic noise measurement techniques, 2003.

Don H. Johnson and Dan E. Dudgeon. *Array Signal Processing: Concepts and Techniques*. Prentice Hall, 1993.

S. Oerlemans and B. Méndez López. Acoustic array measurements on a full scale wind turbine. National Aerospace Laboratory NLR, June 2005.

A. Rogers and J. Manwell. Wind turbine noise issues. *University of Massachusetts*, March 2004.

S. Wagner et al. *Wind Turbine Noise*. Springer, 1996. ISBN 0-387-60592-4.

Wind Power Database. The wind power. Wind turbines and windfarms database. http://www.thewindpower.net/, 2009. Accessed February 2009. Can be found on enclosure CD.

Appendices

Appendix A

Radial Array Optimization

This appendix contains the procedure followed to decrease the number of microphones of a radial array by removing the ones providing redundant information. The radial array depicted in A.1 is optimized in a way that the requirements stated in section 5 are met.

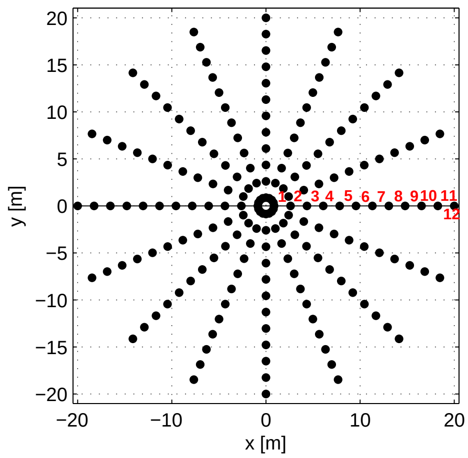

Figure A.1: Microphone disposition of a radial array of 192 microphones with $D = 40$ m, $N = 8$ m and $Ms = 24$. The microphone rings are numbered from the inner to the outer part to illustrate the optimization process.

An optimization process is carried out by systematically remove microphones by rings. This process presents a compromise between resolution and dynamic range, thus both must be evaluated at the same time and any decision to remove a ring must be taken accordingly. The resolution is evaluated for the resolution source scenario (see figure 6.4) through the criteria stated in section 6.2, where the level difference between the weakest source and the minimum towards its adjacent is measured. The MSL is measured simulating the sources 1 and 3 of the MSL scenario (see figure 6.6).

A.1 Removing the Inner Rings

Step 1: First Two Rings Out

It has been observed that removing the microphones of the centre of the array slightly improves the resolution and the dynamic range. Figure A.2 shows the modifications when removing microphones. The resolution improves when the first three rings are removed and the dynamic range improves with the two first rings are eliminated.

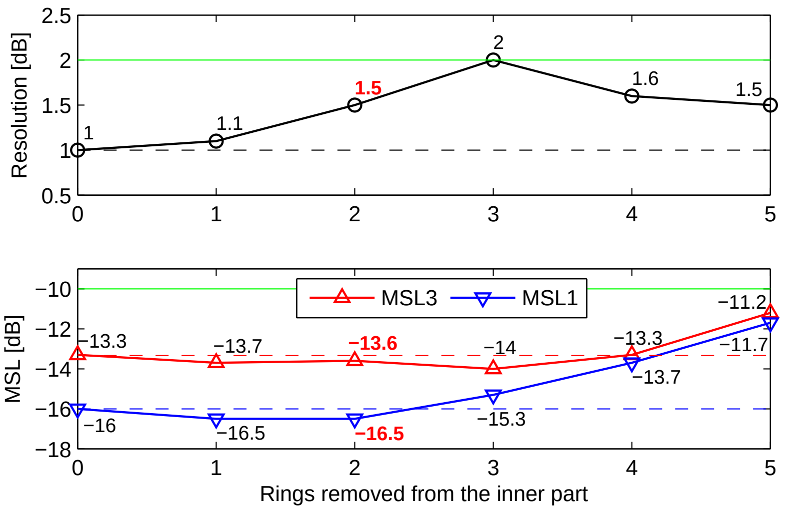

Figure A.2: Changes in resolution and dynamic range of the radial array of figure A.1 when removing rings from the centre increasingly. Dotted lines represent the level without modifications and green lines represent requirement limits: more than 2 dB for resolution and less than −10 dB for the MSL.

It is decided to remove the first two rings preserving a fair dynamic range where the MSL is −16.5 dB and −13.6 dB for sources 1 and 3 of the MSL source scenario respectively. Hence, 32 less microphones are used obtaining slightly better results. Figure A.3 shows the improved geometry and figure A.4 shows simulations results.

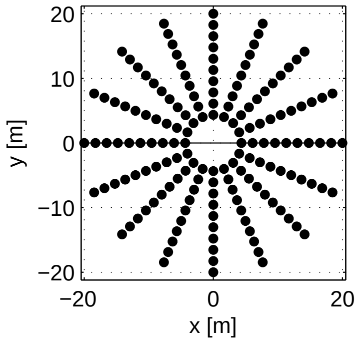

Figure A.3: Microphone distribution the radial array of figure A.1 when the first two microphone rings are removed.

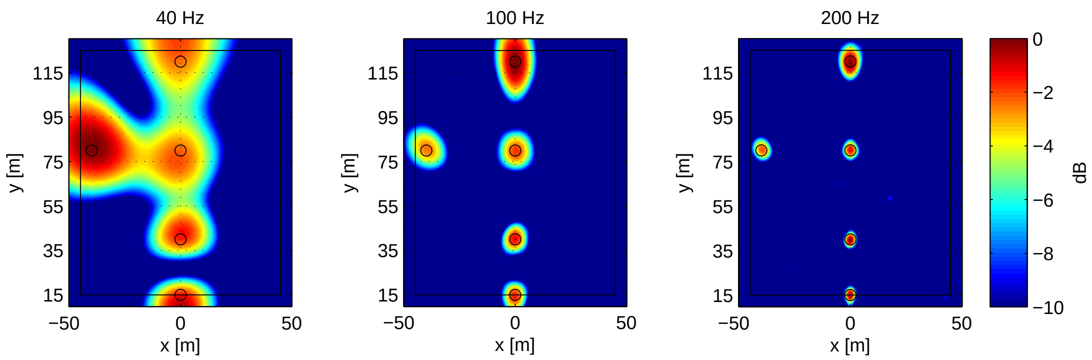

Figure A.4: Acoustic images obtained with the radial array depicted in figure A.3 of 160 microphones with $D = 40$ m, $N = 8$ m, $Ms = 24$, where the first two microphone rings have been removed.

A.2 Removing Rings Systematically

Resolution and dynamic range are measured for each ring that is removed from the radial array depicted in figure A.3. The ring with less influence in the array performance will be eventually removed, then the process is carried out again.

Step 2: Ring Number Five Out

The modifications between the radial array in figure A.3 when removing each of the rings are calculated and depicted in figure A.5.

From the inspection of the data obtained and a visual verification through simulations, it is decided to remove the ring number five, the resulting array is shown if figure A.6.

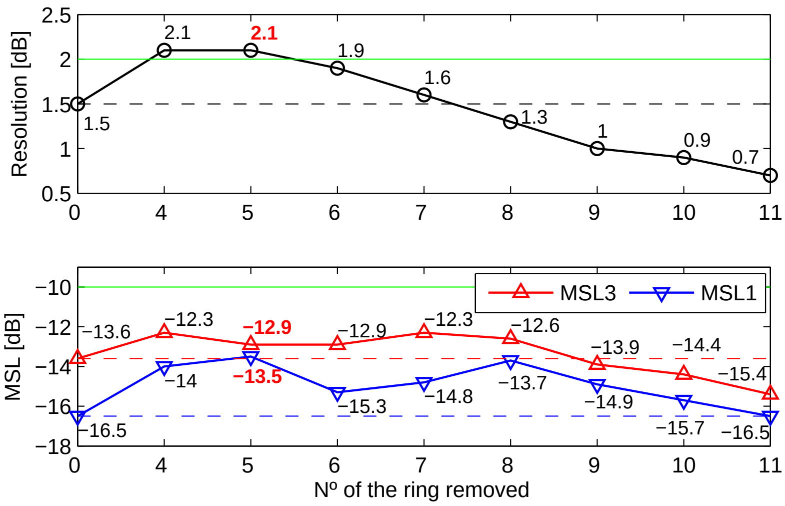

Figure A.5: Changes in resolution and dynamic range of the radial array of figure A.3 (rings 1 and 2 removed) when removing each of the rings of the array separately. Dotted lines represent the level without modifications and the green lines represent requirement limits: more than 2 dB for resolution and less than −10 dB for the MSL.

The resolution is improved now meeting the requirements and the dynamic range is still acceptable. MSL is −13.5 dB and −12.9 dB for sources 1 and 3 of the MSL source scenario respectively.

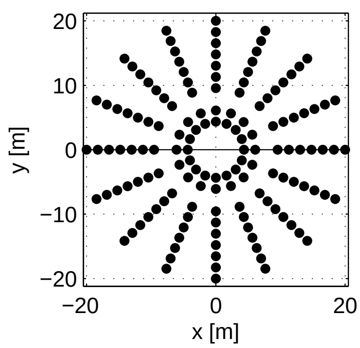

Figure A.6: Microphone distribution the radial array of figure 7.21 when the rings 1, 2 and 5 are removed.

Step 3: Ring Number Seven Out

Again, simulations are carried out removing each ring of the new array and values are modifications are plotted in figure A.7.

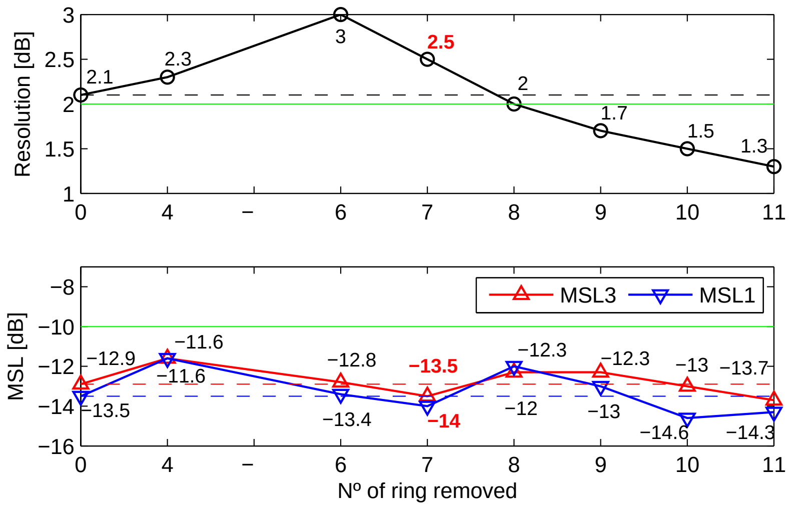

Figure A.7: Changes in resolution and dynamic range of the radial array of figure A.6 (rings 1,2 and 5 removed) when removing each of the rings of the array separately.Dotted lines represent the level without modifications and the green lines represent requirement limits: more than 2 dB for resolution and less than −10 dB for the MSL.

From data obtained in figure A.7 and a visual comparison of the simulations, it is decided to remove the ring number 7, this improves the resolution and leaving MSL values of −14 dB and −13.5 dB for sources 1 and 3 of the MSL source scenario respectively. The resulting array is depicted in figure A.8.

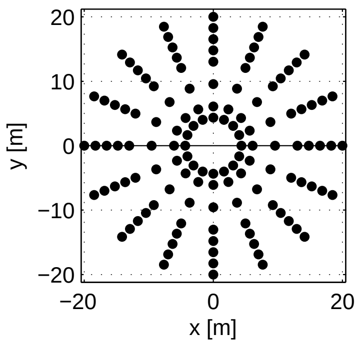

Figure A.8: Microphone distribution of the radial array of figure A.1 when the rings 1, 2, 5 and 7 are removed.

Step 4: Ring Number Three Out

Trough the same procedure the modifications when removing rings from the array depicted in figure A.8 are presented in figure A.9.

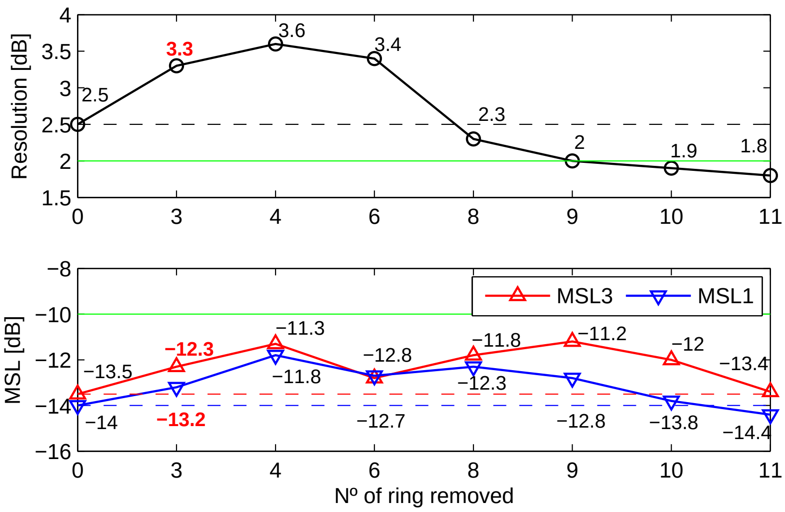

Figure A.9: Changes in resolution and dynamic range of the radial array of figure A.8 (rings 1, 2, 5 and 7 removed) when removing each of the rings of the array separately.

It is decided to remove the ring number 3, this provides better resolution preserving the dynamic range, leaving MSL values of -13.2 dB and -12.3 dB for sources 1 and 3 of the MSL source scenario respectively. The resulting array is shown in figure A.10

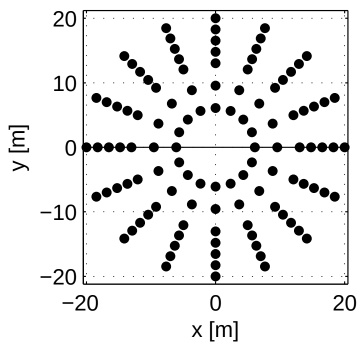

Figure A.10: Microphone distribution the radial array of figure A.1 when the rings 1, 2, 5, 7 and 3 are removed.

Step 5: Ring Number Nine Out

The last ring removed from the array is the ring number 9. It is decided despite results obtained shown in figure A.11 give preference to remove other rings. Acoustic images are inspected, and this option was the best concerning the level homogeneity of the sources, which is important for a fair evaluation of their contribution to the image. The resolution is slightly worsen while it still keeps a good value. The dynamic range decreases but the MLS is still below -10 dB, therefore the requirements are met. Figure A.12 shows the final geometry.

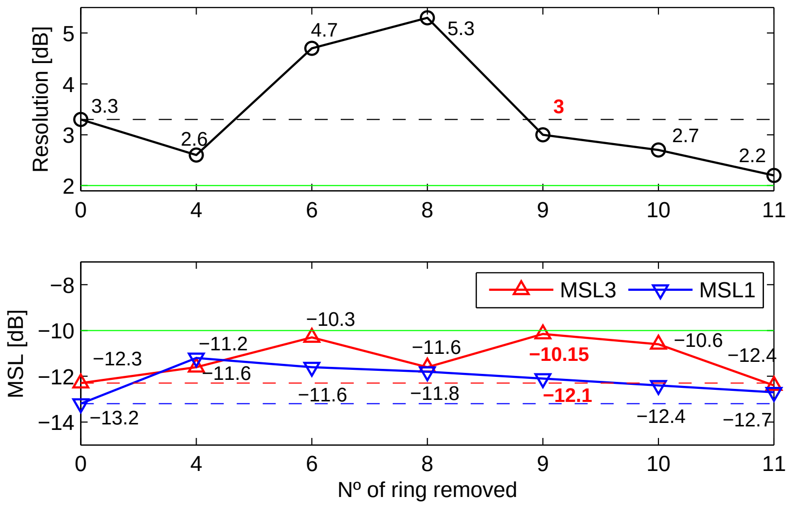

Figure A.11: Changes in resolution and dynamic range of the radial array of figure A.10 (rings 1, 2, 5, 7 and 3 removed) when removing each of the rings of the array separately.

A.3 The Optimized Radial Array

The optimized radial array is depicted in figure A.12 which set-up is:

- Array aperture size: $D = 40$ m.
- Spokes: $N = 8$ m.
- Microphones per spoke: $Ms12$.
- Total number of microphones: $M = 96$.

The results from simulations lead the contour plots shown in figure A.13.

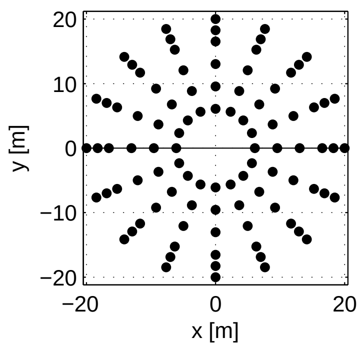

Figure A.12: Microphone distribution the radial array of figure A.1 when the rings 1, 2, 5, 3, 7 and 9 are removed.

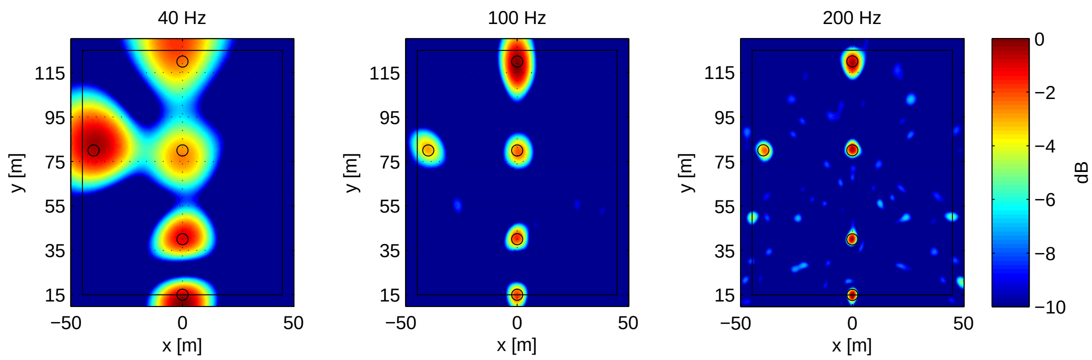

Figure A.13: Acoustic images obtained with the optimized radial array depicted in figure A.12 of 96 microphones with $D = 40$ m, $N = 8$ m, $Ms = 12$.